Asymptotic analysis of the evaporation dynamics of partially wetting droplets

Nikos Savva[1],†, Alexey Rednikov[2] and Pierre Colinet[2]

[1]School of Mathematics, Cardiff University, Cardiff CF24 4AG, UK

[2]Université Libre de Bruxelles, TIPs-Fluid Physics Unit, CP 165/67, 1050 Brussels, Belgium

We consider the dynamics of an axisymmetric, partially wetting droplet of a one-component volatile liquid. The droplet is supported on a smooth superheated substrate and evaporates into a pure vapour atmosphere. In this process, we take the liquid properties to be constant and assume that the vapour phase has poor thermal conductivity and small dynamic viscosity so that we may decouple its dynamics from the dynamics of the liquid phase. This leads to a so-called 'one-sided' lubrication-type model for the evolution of the droplet thickness, which accounts for the effects of evaporation, capillarity, gravity, slip and kinetic resistance to evaporation. By asymptotically matching the flow near the contact line region and the bulk of the droplet in the limit of a small slip length and commensurably small evaporation and kinetic resistance effects, we obtain coupled evolution equations for the droplet radius and volume. The predictions of our asymptotic analysis, which also include an estimate of the evaporation time, are found to be in excellent agreement with numerical simulations of the governing lubrication model for a broad range of parameter regimes.

Key words: condensation/evaporation, contact lines, drops

---

1. Introduction

The evaporation of droplets in contact with solid substrates has been attracting the attention of the scientific community in recent decades, not only due to its presence in nature and technology, but also due to a number of challenging fundamental questions. On the applied front, sessile droplets are important both in emerging domains such as, for example, in digital microfluidics (Choi *et al.* 2012) or DNA analysis (Dugas, Broutin & Souteyrand 2005), and in more traditional application fields such as cooling heat transfer (Kim 2007), micro-deposition and ink-jet printing (Erbil 2012). Also noteworthy is the pioneering work by Deegan *et al.* (1997) on the so-called coffee stain problem, which ultimately triggered intensive research on the effects which control the size and morphology of dried deposits following the evaporation of solutions or dispersion drops (see contributions in Brutin 2015, and the references therein). On the theoretical front, the accurate modelling of droplet

† Email address for correspondence: savvan@cf.ac.uk

spreading and evaporation dynamics still faces considerable difficulties, not only due to the intricate coupling between various effects, but also due to the intrinsic multi-scale nature of problems involving non-equilibrium contact lines.

A substantial body of literature on the subject has been devoted to sessile droplets of pure liquids, studied from two distinct lines of research depending on the nature of the gas phase. When an inert gas such as air is present in the surrounding atmosphere, the droplet evaporation is generally limited by vapour diffusion (see, e.g. Poulard, Guéna & Cazabat 2005; Cazabat & Guéna 2010), and the droplet is only slightly cooled by the latent heat needed for phase change. Yet these small evaporation-induced temperature differences can trigger various types of flows and instabilities (Girard, Antoni & Sefiane 2008; Sefiane *et al.* 2008; Sobac & Brutin 2012), which have been studied by various groups partly in view of their impact on deposition and cleaning processes (Deegan *et al.* 2000; Hu & Larson 2006). There are a number of recent contributions to this first line of research, e.g. on the influence of the substrate thermal conductivity (Ristenpart *et al.* 2007; Dunn *et al.* 2009; Lopes *et al.* 2013), on the details of evaporation-induced flows near the contact line (Gelderblom, Bloemen & Snoeijer 2012), on the effect of convection currents in the gas (Shahidzadeh-Bonn *et al.* 2006; Kelly-Zion *et al.* 2009; Dehaeck, Rednikov & Colinet 2014) as well as on the impact of Marangoni flows on the droplet shape (Tsoumpas *et al.* 2015).

The second line of research concerns pure liquids evaporating into their own vapour in the absence of any other gas. In this case, the dynamics is not limited by diffusion; rather, it is heat transfer and cooling by latent heat that limit the evaporation rate. Generally, it is more difficult to conduct experiments in this configuration due to the technicalities of confining and visualising droplets in a hermetic set-up and, as a result, considerably fewer experimental studies have been reported (Gokhale, Plawsky & Wayner 2003; Sodtke, Ajaev & Stephan 2008; Cioulachtjian *et al.* 2010; Raj *et al.* 2012), noting also the related works on evaporating menisci and condensing droplets within closed cuvettes (Zheng *et al.* 2002; Plawsky *et al.* 2004). From the modelling perspective, the governing equations admit a considerable simplification in this conduction-limited scenario, by invoking the so-called 'one-sided' approximation (Burelbach, Bankoff & Davis 1988). Such models rely on the assumption of a poor thermal conductivity and small dynamic viscosity of the vapour, thus effectively decoupling the vapour phase dynamics from that of liquid. In this manner, evaporation is determined by the amount of heat reaching the liquid–vapour interface only from the liquid side. This approach, used in conjunction with the lubrication hypothesis, underpins most studies on the dynamics of thin evaporating menisci and droplets, both in the complete wetting case (Potash & Wayner 1972; Moosman & Homsy 1980; Ajaev 2005) and in partial wetting situations (Anderson & Davis 1995; Hocking 1995).

Despite this abundant literature on evaporating sessile droplets and, more specifically, on their theoretical modelling, relatively few works deal with the important question of the micro–macro coupling of evaporating droplets which occurs between the small-scale physics prevailing near the contact line and the processes occurring in the bulk of the droplet. The present work is based on an asymptotic matching procedure that relies on a clear separation of the macroscopic scale of an axisymmetric droplet and a microscopic scale relevant to the vicinity of the moving/evaporating contact line. This is a highly non-trivial generalisation of previous analyses with non-volatile droplets (see, e.g. Hocking 1983, 1992) to include evaporation, which will be assumed to be limited mostly by thermal conduction within the drop, i.e. the gas phase is made

of pure vapour (see Savva, Rednikov & Colinet 2014, for a preliminary study on the two-dimensional geometry). Apart from the physical insight gained in understanding the relative importance of the various effects involved at the different scales, such analysis also provides a reduced description of the droplet dynamics in terms of two ordinary differential equations for the droplet radius and volume, which are generally easier to solve numerically compared to the original stiff free-boundary problem as prescribed by the governing partial differential equation and its boundary conditions. To assess the validity of our asymptotic analysis and its regimes of applicability, its predictions are thoroughly scrutinised against the corresponding solutions to the full problem. Noteworthy here are the recent studies by Oliver *et al.* (2015) and Saxton *et al.* (2016), in which similar asymptotic analyses were undertaken, but for different physical settings; the former deals with an imposed uniform mass flux whereas the latter considers an isothermal scenario of diffusion-limited evaporation into an inert gas.

Central to any problem with moving contact lines is the issue associated with the singularity of the viscous stress (Huh & Scriven 1971; de Gennes 1985; Bonn *et al.* 2009) and, possibly here, evaporation-induced singularities (to be discussed hereinafter). Such singularities can be remedied by utilising some contact line model, the most popular of which are based on either relaxing the no-slip condition on the substrate with some slip model (e.g. Lacey 1982; Hocking 1983, 1992) or on disjoining-pressure-induced precursor films, either extended (Schwartz & Eley 1998; Wu & Wong 2004; Eggers 2005a; Yi & Wong 2007; Pismen & Eggers 2008) or truncated to a finite length depending on the spreading parameter (Hervet & de Gennes 1984; de Gennes 1985; Colinet & Rednikov 2011). Although other modelling approaches for the contact line dynamics also exist in the literature including, for example, diffuse interface models (Sibley *et al.* 2013) and the so-called interface formation model (Shikhmurzaev 2008; Sibley, Savva & Kalliadasis 2012), precursor film models have arguably been the most popular choice for exploring numerical solutions to lubrication-type equations with evaporation and other complexities (see, e.g. Ajaev 2005; Sodtke *et al.* 2008; Eggers & Pismen 2010; Murisic & Kondic 2011; Todorova, Thiele & Pismen 2012).

In the present study, we assume that the viscous singularity associated with the motion of the contact line is resolved by the Navier slip. This choice was made partly because it has been traditionally used in the context of partial wetting and partly because of the still-unresolved controversies in disjoining pressure models, such as for example addressing the question whether the disjoining pressure isotherm should be taken to be slope dependent (see, e.g. Wu & Wong 2004). More importantly, a number of studies discuss how the various contact line models can be formally linked through their leading-order asymptotics at the vicinity of the contact line in such a way that they exhibit nearly identical dynamics (King 2001; Eggers 2005a; Savva & Kalliadasis 2011; Sibley *et al.* 2012, 2013, 2015b). Thus, the main features of the dynamics are likely to be qualitatively consistent across all contact line models and, in principle, the analysis undertaken here can be adapted appropriately for any contact line model.

Focusing only on a regime where inertia is negligible and in the absence of evaporation, three, usually distinct, scales/regions may be identified (see, e.g. Bonn *et al.* 2009). Firstly, at scales comparable to the droplet size, capillarity and gravity determine the shape of the droplet (which is taken to be quasi-static at leading order). In this case, microscopic effects, such as disjoining pressure or slip, are negligible
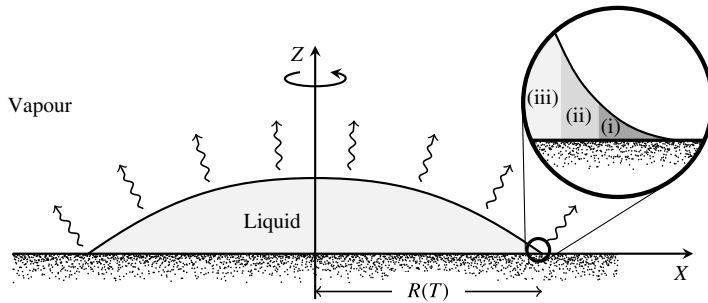
FIGURE 1. Sketch of a thin volatile droplet on a uniformly heated surface in axisymmetric geometry, denoting with $R(T)$ the radius of the circular contact area at time T. The inset shows a zoom into the contact line region, which allows us to distinguish (i) the inner, (ii) the intermediate and (iii) the outer regions over which the asymptotic analysis is undertaken.

and possible flows within the droplet merely induce small corrections to the overall shape. At much smaller scales, near the contact line, gravity is negligible, whereas the previously neglected microscopic effects enter into play and balance the capillary forces together with viscous friction due to contact line motion (see figure 1). Between these two regions lies an intermediate region in which the corresponding free-surface shape is described by the universal Cox–Voinov asymptotics (Voinov 1976; Cox 1986) in such a way that facilitates the matching of the dynamics at the macro- and micro-scale (Hocking 1983). However, direct matching of inner and outer solutions is possible without an intermediate region, provided that the infinite number of non-negligible terms in the far-field expansion of the inner region are properly accounted for (Lacey 1982; Sibley, Nold & Kalliadasis 2015a). In the end, with or without an intermediate region, both approaches yield identical results, as expected.

How evaporation enters/modifies this three-region picture depends crucially on the evaporation regime considered, although we emphasise that a full discussion of the different scenarios is beyond the scope of this study. Here, we focus our attention on the case where evaporation is limited, as previously mentioned, by conduction of heat from the substrate towards the liquid–vapour interface. In the absence of a precursor film as assumed here, this evaporation scenario typically yields unbounded evaporation fluxes at the contact line if the thermal resistance of the liquid formally vanishes. This flux singularity is in practice avoided by considering kinetic effects, the importance of which becomes appreciable at nanoscopic scales (Burelbach *et al.* 1988; Anderson & Davis 1995; Hocking 1995). Yet, it is clear that among the aforementioned asymptotic regions, the inner (micro-) region near the contact line is affected the most by evaporation. In particular, intense microflows generated by a highly localised peak in the evaporation flux near the contact line are known to induce finite apparent contact angles even in the perfectly wetting case (Potash & Wayner 1972; Moosman & Homsy 1980; Stephan & Busse 1992; Morris 2001; Ajaev 2005; Rednikov, Rossomme & Colinet 2009; Todorova *et al.* 2012). In the partial wetting case which is of interest here, the corresponding effect of these flows is a significant increase of the apparent contact angle above the equilibrium value given by Young's equation (Anderson & Davis 1995; Hocking 1995; Colinet & Rednikov 2011; Rednikov & Colinet 2011; Janeček & Nikolayev 2012; Rednikov & Colinet 2013; Saxton *et al.* 2016), noting also that this increase has also been observed

in the context of other models of mass transfer (see, e.g. Davis & Hocking 1999; Oliver *et al.* 2015). A final important remark to make is that although it makes sense to neglect the effect of evaporation on the drop profile at both intermediate (Cox–Voinov) and outer (macro-region) scales, this does not imply that the mass loss due to evaporation at these scales is not appreciable. As we shall see in the following sections, all scales contribute to the global evaporation rate of the drop, whose careful evaluation is an essential feature of this work.

The paper is organised as follows. Section 2 presents the derivation of an evolution equation for the droplet profile under the lubrication approximation with appropriate boundary conditions, and provides the relevant scales, working hypotheses and dimensionless numbers. Section 3 then focuses on the matched asymptotic analysis in the limit of vanishingly small slip lengths, which is used to obtain evolution equations for the droplet radius (§ 3.1) and volume (§ 3.2). Section 4 then presents and discusses the results of a detailed numerical investigation to examine the outcomes of our asymptotic analysis for various sets of parameters. In § 4.1, the stages of the spreading/evaporation process are discussed, focusing on the (typically longer) evaporation stage in § 4.2 and on the derivation of a rather accurate estimate for the total evaporation time. Then, § 4.3 focuses on the case of relatively large kinetic resistance, followed by an investigation on the influence of gravity in § 4.4, including both pendant and sessile droplets. Then, § 4.5 is dedicated to the influence of slip, § 4.6 to the effect of Young's equilibrium contact angle and § 4.7 discusses apparent power-law behaviours observed for the radius and volume of the droplet versus time remaining before complete evaporation. Section 5 then concludes the present work and discusses some possible extensions.

2. Model

Consider the dynamics of an axisymmetric, partially wetting droplet evaporating in its vapour. The droplet is supported on a uniformly heated rigid horizontal surface, which is kept at temperature $\Theta_S = \Theta_0 + \Delta\Theta$, where Θ_0 is the saturation temperature corresponding to the pressure in the vapour phase and $\Delta\Theta$ is the superheat, with $\Delta\Theta \ll \Theta_0$. At time T, the droplet has volume $V(T)$ and wets the substrate over a circular region of radius $R(T)$ (hereinafter referred to simply as the droplet radius). In the present study we assume that the liquid properties, namely the surface tension, σ, density, ρ, and viscosity, μ, all remain constant and utilise the so-called one-sided model proposed by Burelbach *et al.* (1988), which allows us to decouple the dynamics in the vapour phase from that in the liquid.

More specifically, the dynamics of the liquid is treated under the long-wave approximation in the Stokes regime using the (X, Z) coordinate system, where X is the distance from the axis of symmetry of the droplet and Z measures the vertical distance from the substrate (see figure 1). For the liquid flow we have the usual, leading-order lubrication-type equations

$$\partial_Z P = -\rho g, \tag{2.1a}$$

$$\partial_X P = \mu \partial_Z^2 U, \tag{2.1b}$$

$$\partial_X (XU) + X\partial_Z W = 0, \tag{2.1c}$$

where U and W are the velocity components in the X- and Z-directions, respectively, P is the pressure and g the gravitational acceleration. On the substrate ($Z = 0$) we have

$$W = 0, \quad U = b\partial_Z U, \tag{2.2a,b}$$

where b is the slip length, assumed constant. The presence of slip along the substrate alleviates the aforementioned classical stress singularity that occurs at a moving contact line (see §1).

On the free surface $(Z = H)$, we have the tangential and normal stress conditions

$$\partial_Z U = 0, \quad P - P_0 = -\sigma(\partial_X^2 H + X^{-1}\partial_X H), \quad (2.3a,b)$$

respectively, where P_0 is the ambient vapour pressure, assumed constant. Lastly, mass conservation combined with the kinematic boundary condition at $Z = H$ yields

$$\partial_T H + U\partial_X H - W + \rho^{-1}J = 0, \quad (2.4)$$

where $J(X, T)$ is the evaporative mass flux through the liquid–vapour interface (measured in units of mass per unit area per unit time).

The liquid problem is coupled with the temperature field, $\Theta(X, Z, T)$. By neglecting convective heat transport effects, the energy equation reduces in the considered lubrication limit to

$$\partial_Z^2 \Theta = 0. \quad (2.5)$$

Equation (2.5) is solved by taking

$$\Theta = \Theta_S \quad (2.6)$$

on the solid surface $(Z = 0)$; on the droplet surface $(Z = H)$ we have the balance of energy, namely

$$k\partial_Z \Theta + LJ = 0, \quad (2.7)$$

where k is the thermal conductivity of the liquid and L is the latent heat of vaporisation, which reflects the balance of heat conducted through the droplet and the latent heat associated with the phase change occurring at the liquid–vapour interface. Lastly, we employ a constitutive relation arising from kinetic theory (see Schrage 1953), the linearised version of which implies that the deviations of the interfacial temperature from its equilibrium value, Θ_0, are proportional to J according to (see, e.g. Potash & Wayner 1972; Wayner, Kao & LaCroix 1976; Carey 2007; Rednikov *et al.* 2009, and the references therein)

$$J = \frac{\tilde{\rho} f_a L}{\Theta_0^{3/2}(2 - f_a)}\sqrt{\frac{2M_w}{\pi R_g}}(\Theta|_{Z=H} - \Theta_0), \quad (2.8)$$

where M_w is the molecular weight, R_g is the gas constant, $\tilde{\rho}$ is the vapour density and $0 < f_a \leqslant 1$ is the accommodation coefficient, which can be viewed as a measure of the probability that a liquid particle impinging on the liquid–vapour interface enters into the bulk vapour phase (see Paul 1962, for the values of f_a for a number of working fluids).

From these equations, the aim is to obtain an evolution equation for $H(X, T)$ based on the mass balance, equation (2.4), which implies that we need to express the velocities and the evaporative flux in terms of H. To obtain J, we first determine the temperature field from (2.5) and the conditions (2.6) and (2.7), giving

$$\Theta = \Theta_S - LJZ/k. \quad (2.9)$$

Hence, by combining (2.8) and (2.9) we obtain

$$J = \frac{k\Delta\Theta}{L}\frac{1}{s+H}, \tag{2.10}$$

where

$$s = \frac{k\Theta_0^{3/2}(2-f_a)}{\tilde{\rho}f_a L^2}\sqrt{\frac{\pi R_g}{2M_w}} \tag{2.11}$$

is a length scale below which kinetic (non-equilibrium) effects are important. More precisely, for film thicknesses much above that scale, the interface can be assumed to be at the saturation temperature, Θ_0, i.e. a conduction-limited regime. In contrast, for thicknesses smaller than s, deviations from Θ_0 occur while the temperature is uniform across the liquid, i.e. a kinetic- (or reaction-) limited regime. Importantly, as $s \to 0$, J dramatically increases (and diverges) as the contact line is approached, where H vanishes. For $s > 0$, J ultimately saturates for values of H below s (see also the discussion on the limit of large kinetic resistance in §4.3).

In our model we cannot take $s = 0$, because the resulting singularity in J at the contact line is non-integrable. Thus, a non-vanishing kinetic resistance length s is essential to avoid the divergence in J, just as a non-vanishing slip length b is necessary for the resolution of the viscous stress divergence. In contrast, this issue does not arise when precursor films/disjoining pressure models are invoked instead of slip, in which case taking $s = 0$ is allowed in principle (Ajaev 2005; Sodtke *et al.* 2008; Rednikov *et al.* 2009). It is also interesting to note in this context that these non-integrable singularities associated with a moving and/or evaporating contact line can be made integrable by employing a disjoining pressure model based on the classical non-retarded van der Waals interactions (Colinet & Rednikov 2011) or even fully resolved solely by the Kelvin effect accounting for the curvature dependence of the saturation conditions (Rednikov & Colinet 2013). Moreover, integrable singularities in the evaporation flux are also encountered in the case of diffusion-limited evaporation into an inert gas (see Deegan *et al.* 1997; Saxton *et al.* 2016). Clearly there is an abundance of modelling approaches that can be adopted, but here we will stick to (2.10) for describing the evaporation flux, which can be viewed as a key first step in developing an asymptotic framework for investigating more involved evaporation models.

Eliminating the velocities from (2.4) is a matter of standard manipulations utilised in related works (see e.g. Hocking 1983, for the non-volatile case): first eliminate W from (2.4) using (2.1*c*) and (2.2*a*) to obtain

$$\partial_T H + \frac{1}{X}\partial_X\left(X\int_0^H U\,\mathrm{d}Z\right) + \frac{J}{\rho} = 0, \tag{2.12}$$

then derive an expression for P with (2.1*a*) and (2.3*b*) and finally an expression for U using (2.1*b*) together with (2.2*b*) and (2.3*a*),

$$U = -\frac{1}{\mu}\left(\frac{1}{2}Z^2 - HZ - bH\right)\partial_X\left[\sigma\left(\partial_X^2 H + \frac{1}{X}\partial_X H\right) - \rho g H\right]. \tag{2.13}$$

Combining (2.12) together with (2.13) and (2.10) yields the governing equation for the evolution of the droplet thickness, which is cast in dimensionless form as

$$\partial_t h + \frac{1}{x}\partial_x\left\{h^2(h+\lambda)x\partial_x\left(\partial_x^2 h + \frac{1}{x}\partial_x h - Bh\right)\right\} = -\frac{\mathcal{E}}{h+\mathcal{K}}. \tag{2.14}$$

In (2.14) we introduced the dimensionless variables

$$x = \frac{X}{d}, \quad t = \frac{T}{\tau}, \quad h = \frac{H}{d\vartheta_s}, \quad r = \frac{R}{d}, \tag{2.15a-d}$$

with $\tau = 3\mu d/(\sigma\vartheta_s^3)$ being the time scale of capillary action and d the length scale defined by

$$d = \left(\frac{V_0}{2\pi\vartheta_s}\right)^{1/3}, \tag{2.16}$$

for a droplet of reference volume V_0, usually taken to be the volume at $t = 0$. Equation (2.14) depends on four dimensionless parameters, namely

$$\lambda = \frac{3b}{d\vartheta_s}, \quad B = \frac{\rho g d^2}{\sigma}, \quad \mathcal{E} = \frac{3k\mu\Delta\Theta}{\rho \, d\sigma \vartheta_s^5 L}, \quad \mathcal{K} = \frac{s}{d\vartheta_s}, \tag{2.17a-d}$$

where λ is the dimensionless slip length, B is the Bond number comparing gravity to capillarity, $\mathcal{E}$ is the evaporation number, which can be thought of as the ratio of τ and the time scale of evaporation, and $\mathcal{K}$ is the kinetic resistance, which is a non-equilibrium parameter comparing the length scale of kinetic effects with the macroscopic length scale.

In our model, as a first step, we have neglected other effects, such as thermocapillarity, the unsteady heat conduction in the solid or heat losses to the gas phase above the liquid film which were included in a model with a precursor film developed by Sodtke *et al.* (2008). It is also important to note the more involved slip-based model utilised by Anderson & Davis (1995), which, unlike our present treatment, was analysed by assuming *a priori* that the contact line speed is prescribed in terms of a given function of the apparent contact angle.

To solve (2.14), at the contact line, $x = r(t)$, we require that

$$h = 0, \quad \partial_x h = -1, \tag{2.18a,b}$$

so that we have an actual contact line with the free surface meeting the substrate at the (static) Young angle, ϑ_s, which is taken to be small in order to be consistent with the assumptions of the lubrication model. In the non-volatile case, fixing the contact angle is equivalent to having an invariant Hamaker constant and surface tension (see e.g. Savva & Kalliadasis 2011), which is typically assumed to be the case in precursor film models with evaporation. Noteworthy is also that the use of (2.18b) as a boundary condition for slip models has been advocated by Hocking both in the non-volatile (1992) and volatile (1995) cases, arguing that the contact angle variations which are observed in experiments are for the macroscopic, apparent contact angles and arise due to the flow in the vicinity of the contact line region where slip effects are significant.

The above-mentioned conditions are supplemented with appropriate symmetry conditions to be applied at the polar axis, $x = 0$, namely

$$\partial_x h = 0, \quad \partial_x^3 h = 0 \tag{2.18c,d}$$

and the moving boundary condition

$$\dot{r} = -\frac{\mathcal{E}}{\mathcal{K}} + \lambda \lim_{x \to r} h \partial_x^3 h, \tag{2.18e}$$

	Water	Ethanol	Ammonia	FC-72
Θ_0 (K)	373	352	300	305
ρ (kg m^{-3})	960	727	600	1665
$\tilde{\rho}$ (kg m^{-3})	0.6	1.6	9.0	5.7
σ (N m^{-1})	0.059	0.020	0.020	0.010
L ($\times 10^6$ J kg^{-1})	2.3	0.88	1.2	0.091
M_w (kg mol^{-1})	0.018	0.046	0.017	0.338
k (W m^{-1} K^{-1})	0.68	0.17	0.48	0.06
μ ($\times 10^{-4}$ Pa s)	2.8	4.4	1.3	5.9
s (nm)	41.6	15.3	5.3	42.1

TABLE 1. Material properties for various liquids. Data for water and ethanol (at 1 atm) were taken from Burelbach *et al.* (1988); data for ammonia (at 10.5 atm) were taken from Stephan & Busse (1992); data for FC-72 (at 0.40 atm) were taken from Raj *et al.* (2012).

which is derivable directly from a local expansion of (2.14) at the contact line and invoking conditions (2.18*a,b*) (see also Oliver *et al.* 2015, for additional details).

Finally, we define the dimensionless volume of the droplet, $v(t) = V/V_0$, given by

$$v = \int_0^r xh\,dx. \tag{2.19}$$

Clearly, if we multiply (2.14) by x, integrate from 0 to r and use (2.18) we find that

$$\dot{v} = -\mathcal{E} \int_0^r \frac{x}{h + \mathcal{K}}\,dx, \tag{2.20}$$

noting also that initially we typically take

$$v(0) = 1, \tag{2.21}$$

with our chosen non-dimensionalisation if V_0 in (2.16) is to represent the initial droplet volume. However, in some computations we allow for different values of $v(0)$, with V_0 taken to be some reference volume (e.g. to directly compare the evaporation times of droplets of different initial volume, whilst all parameters of the system, including the characteristic length scale, remain constant).

Solving (2.14) and (2.20) for $h(x, t)$ and $v(t)$ subject to the boundary conditions (2.18) and some specified initial conditions (see (C 6) and the discussion in appendix C) results in a nonlinear free-boundary problem. Although its solution can be obtained using purely numerical means, in the following sections we investigate the problem with the method of matched asymptotic expansions, which allows us to obtain a reduced problem consisting of a set of evolution equations for the droplet volume, $v(t)$, and radius, $r(t)$.

To get a sense of the relative size of the various non-dimensional parameters and to motivate the asymptotic analysis to be developed, let $b = 1$ nm, $\Delta\Theta = 1$ K, $d = 1$ mm, $f_a = 1$ (ideal evaporation scenario) and use the parameter values for various fluids listed on table 1. If we take $\vartheta_s = 8°$, we get $\lambda = 2.1 \times 10^{-5}$ and the following pairs of approximate values for $(\mathcal{E}, \mathcal{K})$: $(8.3 \times 10^{-5}, 29.8 \times 10^{-5})$ for water; $(33.0 \times 10^{-5}, 10.9 \times 10^{-5})$ for ethanol; $(24.5 \times 10^{-5}, 3.8 \times 10^{-5})$ for ammonia; $(132 \times 10^{-5}, 30.1 \times 10^{-5})$ for perfluorohexane (FC-72). When $\vartheta_s = 4°$, the values of λ and $\mathcal{K}$ become twice as large compared to the previous sets of parameter values, whereas the values of $\mathcal{E}$ become 32 times larger. Clearly, since $\mathcal{E}$ scales with $\Delta\Theta$

and ϑ_s^{-5}, we can obtain comparatively larger values of $\mathcal{E}$ at higher superheats and smaller contact angles, subject to the caveat that the constitutive law (2.8) relies on the assumption of weak evaporation rates and $\Delta\Theta \ll \Theta_0$.

It should be emphasised here that the values of the parameters reported above are only indicative of their sizes, especially because the length scale s can lie in a much wider range of values due to the difficulties associated with the experimental determination of f_a. Thus, the presence of contaminants, the sensitivity of f_a on pressure and/or temperature variations and the difficulties in measuring the temperature jumps across the vapour–liquid interface with high accuracy can be some of the contributing factors for the scatter of data across experiments reported in the literature (e.g. for water, f_a was found to range somewhere between 0.01 and 1 in the relatively more recent experiments; see Eames, Marr & Sabir 1997; Marek & Straub 2001; Davidovits *et al.* 2004, for reviews). Hence accounting for this variation in f_a, the values of s (or, equivalently, $\mathcal{K}$) given above can undergo a hundredfold increase, thus becoming comparable or even larger than the slip length, b (or, equivalently, λ), which, in turn, can undergo a hundredfold or more increase if one accounts for the variations in the values of b reported in the literature (typically, $b \approx 1$ nm–1 µm; see Lauga, Brenner & Stone 2007).

From the above discussion, one can readily conclude that the parameters λ, $\mathcal{E}$ and $\mathcal{K}$ are typically small, which means that we deal with macroscopically large drops where evaporation occurs at a time scale that is much longer compared to τ. Thus, in order to develop a consistent asymptotic analysis based on only one small parameter, we introduce the modified evaporation number, $E = \lambda^{-1}\mathcal{E}$ and the modified kinetic resistance $K = \lambda^{-1}\mathcal{K}$, so that λ is always the small parameter of the problem. However, based on the discussion of the preceding paragraphs, this rescaling amounts to having the values of E and K span a few orders of magnitude. The analysis that follows is undertaken in the limit as $\lambda \to 0$ and, in the distinguished limit we are investigating here, the evaporation term in (2.14) becomes important only within a small region near the contact line, as is the case with slip (see, e.g. Hocking 1983). This limits the focus of the present study up to values of E which are moderately large, although, as we shall see, the predictions of the analysis compare rather favourably with full numerical simulations for much larger values of E as well. We consider moderate gravitational effects, so that B is assumed to be $O(1)$. Lastly, as we shall see, the analysis is valid for small to moderately large values of $K > 0$, although the limit $K \gg 1$ so that $\mathcal{K} = O(1)$ will also be explored.

3. Asymptotic analysis

A brute force numerical approach, in which $h(x, t)$, $r(t)$ and $v(t)$ are determined directly by solving the model under consideration, reveals that droplets typically undergo a four-stage process, each valid at a different time scale (further details are given in §4.1). Qualitatively, the predictions of the present model are equivalent to those seen in the model investigated by Saxton *et al.* (2016) for the diffusion-limited evaporation scenario. For $t = O(1)$, the details of the macroscopic initial free-surface shape are lost, as the shape relaxes to a quasi-static profile (see (3.4)). This stage turns out be too brief to have an impact on the dynamic behaviours that follow (see also the computations by Savva & Kalliadasis 2012; Ren, Trinh & Weinan 2015, for non-volatile droplets). In fact, we expect the volume of the droplet to be conserved and the contact line to remain stationary at leading order (see also Saxton *et al.* 2016). For these reasons, considering in detail the early stages is perhaps not worth the additional effort required since this would involve, for the most part, a numerical treatment.

During the second stage (the spreading stage), the contact line moves an order unity distance either by advancing or by receding towards an apparent contact angle, denoted by ϑ_m, which can be quite different from ϑ_s. This difference is attributed to the evaporation-induced contributions into the apparent contact angle and become more pronounced for stronger evaporation fluxes near the contact line (see, e.g. Stephan & Busse 1992; Rednikov & Colinet 2011; Janeček & Nikolayev 2012; Saxton *et al.* 2016). We will see shortly that, consistently with Saxton *et al.* (2016), there is no appreciable mass loss during this stage either. For this reason, it is natural to anticipate that the spreading stage occurs on the same time scale as the spreading time scale of non-volatile droplets, namely $t = O(|\ln \lambda|)$ as $\lambda \to 0$ (Lacey 1982; Hocking 1983).

The third stage, during which the droplet loses an order-unity volume due to evaporation will turn out to occur at the much longer time scale $t = O(1/(\lambda|\ln \lambda|))$ as $\lambda \to 0$ (see § 3.2). Later on, we will argue that a specialised asymptotic treatment of this evaporation stage is not necessary and avoids the intricacies of constructing a composite asymptotic expansion that encompasses all the relevant time scales of the problem. Lastly, during the fourth and final stage of the dynamics, the droplet is close to extinction. We do not have a clear separation of length scales since λ becomes comparable to the droplet size and undertaking an asymptotic analysis close to extinction is no longer possible.

Thus, in the analysis that follows, we focus on the second stage of the dynamics, also implying that the leading-order dynamics of the evaporation stage is described by the same equations. We will extend the work of Hocking (1983) on non-volatile droplets to obtain an equation for $\dot{r}(t)$ that accounts for the evaporative term appearing in (2.14), which will then be complemented with an appropriate equation for $\dot{v}(t)$.

3.1. *Evolution of the droplet radius*

Obtaining an evolution equation for the droplet radius, $r(t)$, is carried out in the same fashion as in related studies involving contact line dynamics without evaporation (see e.g. Hocking 1983; Savva & Kalliadasis 2009; Vellingiri, Savva & Kalliadasis 2011; Savva & Kalliadasis 2012, 2013), whereby we treat the bulk of the liquid drop separately from the region in the vicinity of the contact line. In the central region of the droplet, the outer region, slip and evaporation-induced free-surface deformations are neglected, but they become important near the contact line. Gravitational effects are important at the onset in the outer region only, since they diminish as the droplet becomes smaller due to evaporation.

3.1.1. *Outer region*

The analysis of the outer region is nearly identical to the analysis undertaken by Hocking (1983), the main difference being the time variation of the droplet volume. Here we reiterate the main results, albeit with a slightly different notation, referring the interested reader to the original work of Hocking for further details. The rate of spreading $\dot{r}$ is assumed to be small, so that we may employ the quasi-static approximation, introducing the expansion

$$h_{out} \sim h_0(x, r, v) + \dot{r} h_1(x, r, v) + \cdots, \tag{3.1}$$

i.e. time enters the problem through v, r and $\dot{r}$. Anticipating the scalings for $\dot{r}$ and $\dot{v}$ determined later on, we find that, as $\lambda \to 0$, $\dot{r} = O(1/|\ln \lambda|)$ (as in the non-volatile

case) and $\dot{v} = O(\lambda|\ln\lambda|)$ (as will follow from the analysis of (2.20)). Hence, although $\dot{r}$ is small, it is nonetheless generally much greater than λ and $\dot{v}$ and is accordingly treated as such. Thus, we neglect the evaporation and slip effects in the outer region, so that h_{out} satisfies at $O(\lambda^0)$

$$\partial_t h_{out} + \frac{1}{x}\partial_x \left\{ h_{out}^3 x \partial_x \left(\partial_x^2 h_{out} + \frac{1}{x}\partial_x h_{out} - B h_{out} \right) \right\} = 0. \tag{3.2}$$

Collecting powers of $\dot{r}$ in (3.2) gives

$$\partial_x \left(\partial_x^2 h_0 + \frac{1}{x}\partial_x h_0 - B h_0 \right) = 0 \tag{3.3}$$

to $O(\dot{r}^0)$. This is a third-order differential equation, and is solved subject to (2.18a), (2.18d) and (2.19). The solution to (3.3) is given in terms of modified Bessel functions as

$$h_0 = \frac{\theta}{\sqrt{B}} \frac{I_0(c) - I_0(x\sqrt{B})}{I_1(c)}, \tag{3.4}$$

where $c = r\sqrt{B}$ and θ is the apparent contact angle, defined as

$$\theta = \frac{2v\sqrt{B}I_1(c)}{r^2 I_2(c)}. \tag{3.5}$$

Note that θ corresponds to a rescaled angle, which needs to be multiplied by ϑ_s to obtain the true one. When $B = 0$, equations (3.4) and (3.5) reduce to

$$h_0 = \frac{\theta r}{2} \left(1 - \frac{x^2}{r^2} \right) \quad \text{and} \quad \theta = \frac{8v}{r^3}, \tag{3.6a,b}$$

respectively. From the $O(\dot{r})$ terms in (3.2) we find that h_1 must satisfy

$$\partial_r h_0 + \frac{1}{x}\partial_x \left\{ h_0^3 x \partial_x \left(\partial_x^2 h_1 + \frac{1}{x}\partial_x h_1 - B h_1 \right) \right\} = 0, \tag{3.7}$$

obtained by taking $\partial_t h_0 = \dot{r}\partial_r h_0$. Multiplying both sides by x and integrating yields

$$\partial_x \left(\partial_x^2 h_1 + \frac{1}{x}\partial_x h_1 - B h_1 \right) = \frac{r^3 I_1(c) I_2(c)[x I_1(c) - r I_1(x\sqrt{B})]}{4v^2 [I_0(c) - I_0(x\sqrt{B})]^3}. \tag{3.8}$$

This is also a third-order differential equation solved subject to homogeneous boundary conditions, namely $h_1 = 0$ at $x = r(t)$, $\partial_x h_1 = 0$ at $x = 0$ and $\int_0^r x h_1 \, dx = 0$. Here we are merely interested in obtaining the behaviour of the slope of h_1 as the contact line is approached. Following Hocking (1983), the slope has the asymptotic form

$$-\partial_x h_1 \sim \frac{1}{\theta^2} \ln \left[\frac{e^2}{\delta} \left(1 - \frac{x}{r} \right) \right] \tag{3.9}$$

as $x \to r$, where δ is determined from

$$\ln\delta = \int_0^1 x \left\{ \frac{c I_1^3(c)[x I_1(c) - I_1(xc)]^2}{I_2^2(c)[I_0(c) - I_0(xc)]^3} - \frac{1}{1-x} \right\} dx, \tag{3.10}$$
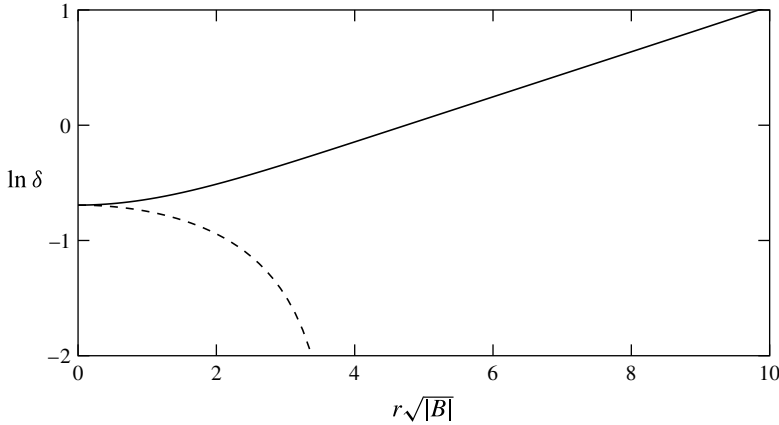
FIGURE 2. Dependence of $\ln \delta$ on $r\sqrt{|B|}$ for a sessile ($B > 0$; solid curve) and a pendant ($B < 0$; dashed curve) droplet. As the droplet evaporates, $r \to 0$, the curves approach asymptotically the value of $\ln \delta = -\ln 2$, corresponding to the $B = 0$ case.

which changes with r and needs to be evaluated numerically. In (3.9), $O(x - r)$ terms are neglected and, just as in many instances throughout the manuscript, the constant terms are absorbed into the logarithmically diverging term. It is important to emphasise that although the above analysis concerns sessile droplets (with $B > 0$), the extension to pendant droplets (with $B < 0$) is trivial and one needs to replace the modified Bessel functions with Bessel functions, take $c = r\sqrt{-B}$ throughout and change the sign of the first term in braces in (3.10), keeping also in mind that sufficiently large pendant droplets may possibly detach from the substrate. Thus, since our model does not account for the detachment dynamics of pendant droplets, we restrict our treatment to pendant droplets for which c is always less than the limiting value of c, the first positive root of the Bessel function J_1. When c attains this value, the denominator of (3.4) vanishes when modified appropriately for pendant droplets. Figure 2 shows a plot of $\ln \delta$ as a function of $r\sqrt{|B|}$ for both pendant and sessile droplets. As expected, we see that as the droplet evaporates so that $r \to 0$, the effect of gravity on the value of δ diminishes and $\delta \to 1/2$, the zero Bond number limit. For pendant droplets, there is a vertical asymptote near 3.83, the first positive root of J_1.

Hence, the asymptotics of the slope of the free surface as $x \to r$ can be readily obtained by combining (3.4) and (3.9):

$$-\partial_x h \sim \theta + \frac{\dot{r}}{\theta^2} \ln \left[\frac{e^2}{\delta} \left(1 - \frac{x}{r} \right) \right]. \tag{3.11}$$

This behaviour is to be matched, within an appropriate overlap region, with the corresponding behaviour of the inner region.

3.1.2. *Inner region*

Whilst considering the solution in the outer region, we did not use the contact angle condition, equation (2.18b), which can only be applied in the inner region, where slip and evaporation effects become important. From the inner region near the contact line, we anticipate a behaviour that allows the matching with the outer-region dynamics as we move away from the contact line.

To investigate the inner-region dynamics, introduce the change of variables

$$\eta = \frac{r - x}{\lambda} \quad \text{and} \quad \phi = \frac{h}{\lambda}, \tag{3.12a,b}$$

which allows us to write (2.14) as

$$\dot{r}\partial_\eta\phi + \partial_\eta[\phi^2(\phi + 1)\partial_\eta^3\phi] = -\frac{E}{\phi + K} \quad \text{for } \eta > 0, \tag{3.13}$$

where we have retained $O(\lambda^0)$ terms only, neglecting $O(\lambda^2 B)$ terms for moderate gravitational effects. The boundary conditions to be applied are $\phi = 0$ and $\partial_\eta\phi = 1$ at $\eta = 0$ and, in order to match with (3.11), $\partial_\eta\phi$ must be no more than logarithmically large as $\eta \to \infty$. Note that (3.13) arises in the two-dimensional geometry as well (Savva *et al.* 2014), which is not surprising given that the contact line appears to be a straight line in its immediate vicinity when $r \gg \lambda$.

Generally, the evaporative flux terms are comparable to the capillary terms and need to be retained in the leading-order equations (see also appendix A, where the case $E \ll 1$ is explored). To proceed, just like the outer region, consider a small-$\dot{r}$ expansion in (3.13) of the form

$$\phi \sim \phi_0 + \dot{r}\phi_1 + \cdots. \tag{3.14}$$

At leading order in $\dot{r}$, (3.13) gives

$$\partial_\eta[\phi_0^2(\phi_0 + 1)\partial_\eta^3\phi_0] = -\frac{E}{\phi_0 + K}, \tag{3.15}$$

which is solved for $\eta > 0$ subject to

$$\phi_0 = 0 \quad \text{and} \quad \partial_\eta\phi_0 = 1 \tag{3.16a,b}$$

at $\eta = 0$ and requiring that ϕ_0 behaves linearly at infinity, namely

$$\phi_0 \sim \theta_m\eta \quad \text{as } \eta \to \infty, \tag{3.16c}$$

where θ_m is the (rescaled with ϑ_s) macroscopic Young's angle modified by evaporation. As it turns out, θ_m is a degree of freedom arising from the far-field expansion of the problem and needs to be determined for given values of E and K. Thus, solving (3.15) with (3.16) numerically allows us to extract the value of θ_m (see appendix B.1 for details).

Figure 3 summarises some representative computations performed for θ_m and its asymptotics. Figure 3(*a*) shows the dependence of θ_m with E for different values of K. For small values of E, the curves obtained from the full problem (3.15)–(3.16) are tangential to the asymptotic result deduced in appendix A for weakly modified θ_m, see (A 5) with (A 8), and is shown as dashed lines. Figure 3(*b*) shows plots of θ_m as K is varied between 0.1 and 25 for different values of E. As K increases, θ_m gradually approaches Young's angle. For the smaller values of E we have good agreement between the full numerics (solid curves) and the asymptotic result (A 5) with (A 8) (dashed curves), which improves as K is further increased. When $E = 10$ and $E = 100$, the small-E asymptotic result, equation (A 5) with (A 8), over-predicts θ_m and for this reason these curves are discarded. This is to be expected given that these values of E cannot possibly conform with the conditions stated in appendix A,
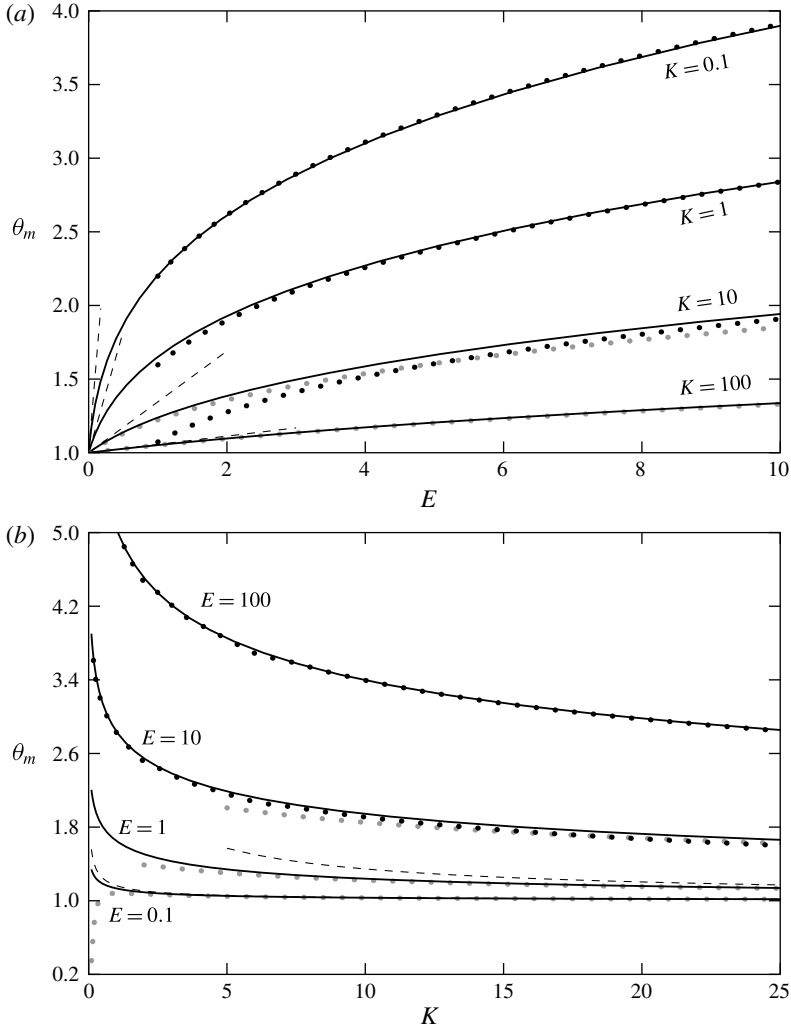
FIGURE 3. (*a*) Plots of θ_m as a function of E for various values of K. (*b*) Plots of θ_m as a function of K for various values of E. The solid curves correspond to the values of θ_m obtained by solving (3.15)–(3.16); the dashed curves correspond to the asymptotic result for $E \ll 1$, equation (A 5) with (A 8); the black dotted curves show the asymptotic behaviour $\theta_m \sim \zeta(K)E^{1/4}$ as $E \to \infty$; the grey dotted curves show the result of Hocking's asymptotics, equation (3.17). The asymptotic results are only shown for the cases where their applicability can reasonably be expected.

which are necessary for the asymptotic result to hold. From these plots it is clear that θ_m increases as E increases and as K decreases. Thus evaporation enhances θ_m but its effect is diminished if the kinetic resistance effects become too large. These results are consistent, at least qualitatively, with those of Rednikov *et al.* (2009), who used a disjoining pressure model for the contact line dynamics, the main difference being the presence of a weak singularity of θ_m in the present model, manifested as $K \to 0$.

As $E \to \infty$, we find that $\theta_m \gg 1$ and θ_m tends asymptotically to $\zeta(K)E^{1/4}$, where $\zeta(K)$ is a function of K to be determined numerically (see appendix B.2). In this limit,

we find that the original, non-scaled, evaporation-modified Young's angle, $\vartheta_m = \theta_m \vartheta_s$, will no longer depend on the actual value ϑ_s, because E scales with ϑ_s^{-4}. The results corresponding to the strong-evaporation result, $\theta_m = \zeta(K)E^{1/4}$, are represented in figure 3 as black dotted curves and appear to yield a very good estimate even for $E = O(1)$, provided that K is sufficiently small. Noteworthy is also that similar $E^{1/4}$ power-law behaviours in evaporation-modified angles have also been reported in different evaporation settings, e.g. by Morris (2001) in a setting which is equivalent to taking $K \gg 1$ (see also Todorova *et al.* 2012), but not in an explicit context of weak or strong evaporation, and also by Rednikov *et al.* (2009) in the weak evaporation limit for a different model. Interestingly, the recent analysis of Saxton *et al.* (2016) uncovered a remarkably similar, $E^{2/7}$ power-law behaviour in the diffusion-limited evaporation scenario with $E \gg 1$.

It is important to note that evaporation-modified contact angles have also been considered in a similar setting by Hocking (1995) and it is thus of interest to put his findings in the present context. More specifically, motivated by the work of Anderson & Davis (1995), Hocking focused on steady two-dimensional droplet shapes in which the fluid lost due to evaporation was replaced by a flux of fluid through the substrate so that there was no contact line motion and no volume variations. He used the same ingredients for evaporation as here, but retained the evaporative term in his outer-region analysis, which is neglected here. Another key difference is the assumed order of magnitude of the kinetic resistance to evaporation. Here, this non-equilibrium effect is treated to be small and only appreciable in the vicinity of the contact line, just as slip is. In contrast, Hocking (1995) formally treated the kinetic resistance to be significant at the macro-scale, although in the end he aimed at the small-K limit (in his terms). Hence, unsurprisingly, Hocking needed to obtain the evaporation-modified angles from the coupling of the micro- and macro-scales, unlike here, where θ_m is solely determined from the inner-region asymptotics. Clearly, Hocking's asymptotic treatment and ours correspond to two distinct parameter regimes, neither of which is a particular case of the other. Nevertheless there can exist a region in the parameter space where the two asymptotic cases overlap, when the kinetic resistance is small compared to the baseline case of Hocking (1995), but large in terms of the present study, i.e. when $K \gg 1$ and $\lambda K \ll 1$. The overlap region in question is described by Hocking's (1995), equation (14), where we note a typo in the denominator of the logarithmic term, with the factor 2 to be replaced by 3. When rendered in our notation and scalings and with the typo rectified, equation (14) in Hocking (1995) can be written as

$$\theta_m^4 = 1 + \frac{4E}{K} \ln \frac{eK}{\theta_m}, \qquad (3.17)$$

which is a transcendental equation for θ_m. In accordance with Hocking's derivation, equation (3.17) is valid, in our terms, for $K \gg 1$ and $E/K \ll 1$ and generally for $(E/K) \ln K = O(1)$, allowing for $O(1)$ deviations from Young's angle, scaled to unity here. In a sense, equation (3.17) can be viewed as the counterpart of the work of Morris (2001) carried out in the limit $K \gg 1$. Although, as we mentioned, equation (3.17) still holds when $\theta_m - 1 = O(1)$, it simplifies to $\theta_m = 1 + (E/K) \ln(eK)$ in the particular case $\theta_m - 1 \ll 1$. This two-term asymptotic result matches perfectly with our result for weakly evaporation-modified angles, equation (A 5), when α, given by (A 8), is expanded for $K \gg 1$. To demonstrate this overlap, Hocking's asymptotic result, equation (3.17), is represented in figure 3 by grey dotted curves and is seen to agree well within the domain of its validity with the full computation result (solid curves).

Looking at the $O(\dot{r})$ terms of (3.13) using (3.14) gives a linear problem to determine ϕ_1,

$$\partial_\eta \phi_0 + \partial_\eta [\phi_0^2(\phi_0 + 1)\partial_\eta^3 \phi_1 + \phi_0(3\phi_0 + 2)\phi_1 \partial_\eta^3 \phi_0] = \frac{E\phi_1}{(\phi_0 + K)^2}, \qquad (3.18)$$

which is treated with homogeneous conditions at $\eta = 0$,

$$\phi_1 = \partial_\eta \phi_1 = 0 \qquad (3.19a)$$

and by requiring that $\partial_\eta \phi_1$ is no more than logarithmically large as $\eta \to \infty$, where the last condition and the asymptotics of (3.18) and ϕ_0 dictate that

$$\partial_\eta \phi_1 \sim \frac{1}{\theta_m^2} \ln \beta\eta \quad \text{as } \eta \to \infty. \qquad (3.19b)$$

Here, β is a degree of freedom which needs to be determined as part of the solution for given values of E and K (see appendix B.3 for a brief discussion on the implementation of the numerical scheme for ϕ_1).

Combining (3.16c) and (3.19b) and going back to the original variables, we find

$$-\partial_x h \sim \theta_m + \frac{\dot{r}}{\theta_m^2} \ln \left(\beta \frac{r - x}{\lambda} \right) \quad \text{as } (r - x)/\lambda \to \infty, \qquad (3.20)$$

which is to be matched with the asymptotics of the outer solution, (3.11). It is clear from (3.20) that λ/β is a measure of the size of the inner region and it is thus of interest to explore how β varies as a function of E and K. Figure 4 shows plots of $\ln \beta$ as E and K are varied and, unlike the corresponding plots of θ_m, the dependence on these parameters is non-monotonic. In figure 4(a) $\ln \beta$ exhibits an initial decrease followed by an increase as E becomes large, but this behaviour is delayed for large K. A similar behaviour is observed in figure 4(b) as K is varied while E is kept constant, but we now have that $\ln \beta \to 1$ as $K \to \infty$, which corresponds to the non-volatile case (Hocking 1983). The approach to this asymptotic behaviour becomes more gradual for larger values of E.

At this point, we note that the differences in the contact line model employed, be it a precursor or a slip model, will only manifest themselves in the inner-region dynamics, when the droplet is sufficiently large. Thus, had we used, for example, a disjoining pressure model in our formulation we would have anticipated the same behaviour as in (3.20) with the slip length being replaced by the associated micro-scale of the disjoining pressure model, say, the thickness of the precursor film (Savva & Kalliadasis 2011) or a length scale obtained by the Hamaker constant, surface tension and the contact angle (Colinet & Rednikov 2011). Similar conclusions can also be drawn with other popular contact line models (see, e.g. Sibley *et al.* 2012, 2013, 2015b).

3.1.3. *Matching*

One readily observes that the outer solution, equation (3.11), cannot match with the inner one, equation (3.20), since the x-dependent logarithmic terms have different coefficients. This issue can be resolved with an intermediate layer sandwiched between the inner and outer regions as shown in figure 1 (Hocking 1983). As noted in previous studies (see, e.g. Savva & Kalliadasis 2009; Sibley *et al.* 2015a), this intermediate
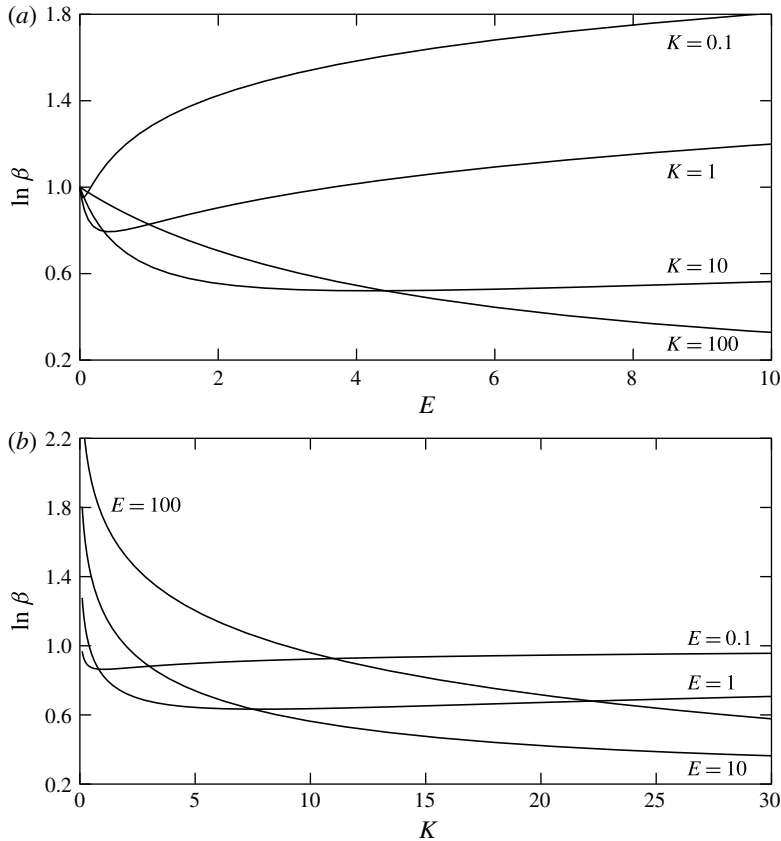
FIGURE 4. (*a*) Plots of $\ln \beta$ as a function of E for various values of K. (*b*) Plots of $\ln \beta$ as a function of K for various values of E.

region ultimately justifies why matching can be carried out simply by considering the cubes of the outer and inner slopes, equations (3.11) and (3.20), respectively. Matching inner and outer solutions can be accomplished without an intermediate region by an alternative path originally proposed by Lacey (1982). In this case, matching is performed not only for the first few terms of the asymptotic expansion, but effectively for the infinite series of the inner and outer solutions (for a discussion placed in the context of contact line motion with mass transfer, see the work of Oliver *et al.* 2015). In a more recent development, Sibley *et al.* (2015*a*) discuss this alternative method of matching inner and outer solutions for contact line motion in a more general setting, explaining how it can be performed in a straightforward manner for more complicated problems for which simply considering the cubes of the slopes argument does not work. As expected, however, both approaches yield the same results.

In the present problem, considering the cubes of (3.11) and (3.20) does allow us to cancel the x-dependent logarithmic terms and by matching the terms that are constant in x we obtain the following evolution equation for the droplet radius

$$\dot{r} = \frac{\theta^3 - \theta_m^3}{3 \ln \dfrac{\beta \delta r}{\lambda e^2}}, \tag{3.21}$$

which is valid for $\dot{r} = O(1/|\ln \lambda|)$ and is determined with $O(1/|\ln \lambda|^3)$ error as $\lambda \to 0$. Although a detailed consideration of an intermediate region is omitted here, as done, for example in other works studying contact line motion in different settings (see, e.g. Eggers 2005*b*; Savva & Kalliadasis 2014; Xu & Jensen 2016), the matching procedure can be rigorously justified by following nearly identical arguments as the ones presented in the above-mentioned works.

Equation (3.21) tells us that the contact line will move an order-unity distance within $t = O(|\ln \lambda|)$ as $\lambda \to 0$, but we will also argue heuristically later on (see § 4.2) that it can be extended to the evaporation stage as well. Before continuing with our analysis, we remark that a similar analysis undertaken by Anderson & Davis (1995) with a one-sided evaporation model assumed as a starting point a functional relation between $\dot{r}$ and θ; here (3.21) is the outcome of the matched asymptotic analysis we have undertaken. Moreover, recall that the θ_m^4 law obtained through matching by Hocking (1995), equation (3.17), is for evaporation-modified angles and not for motion-modified ones, which results to a θ^3 term, as seen in (3.21). Lastly, we note that an analogous result was obtained by Saxton *et al.* (2016) in the diffusion-limited evaporation case, but without the $O(1/\ln^2 \lambda)$ terms as retained here.

On the other hand, an asymptotically consistent expansion for $\dot{r}$ in which $O(1/\ln^2 \lambda)$ terms are retained requires, in principle, the inclusion of an $O(1/|\ln \lambda|)$ correction to $r(0)$ to be used as an initial condition to (3.21), as compared to the value of $r(0)$ for the full problem. This correction would arise from a (mostly numerical) treatment of the capillary action stage which occurs for $t = O(1)$ (see also Oliver *et al.* 2015; Ren *et al.* 2015; Saxton *et al.* 2016). Yet, although our simulations repeatedly show that the capillary action phase and the initial droplet profile are unimportant for the subsequent dynamics, one can take the $r(0)$ correction to be *a priori* negligibly small by considering initial drop shapes which are already sufficiently close to the quasi-static profiles, equation (3.4).

3.2. *Evolution of the droplet volume*

Equation (3.21) depends on the droplet volume, $v(t)$, through the expression for θ, equation (3.5). Hence, to close the system, we will utilise (2.20) to obtain an evolution equation for $\dot{v}$ in terms of $r(t)$, $v(t)$ and the system parameters, $\mathcal{E}$, $\mathcal{K}$, λ and B.

As a first approximation, we may assume that the fine details coming from the contact line region are negligible. Hence, we may take

$$\dot{v} = -\int_0^r \frac{\mathcal{E}x}{h_0 + \mathcal{K}} \, \mathrm{d}x, \tag{3.22}$$

where h_0 is the leading-order outer solution, equation (3.4). This expression is not amenable to further analysis and one needs to compute this integral at each time, unless we consider the $B = 0$ case, so that we may use (3.6*a*) for h_0 in (3.22) to obtain

$$\dot{v} = -\frac{\mathcal{E}r}{\theta} \ln\left(\frac{\theta r}{2\mathcal{K}} + 1\right). \tag{3.23}$$

From (3.23) we can easily deduce that $\dot{v} = O(\lambda|\ln \lambda|)$ as $\lambda \to 0$ for moderate values of E and K. However, equation (3.23) is not expected to work well for all the parameter regimes of interest. The reason is because the influence of the inner region near the contact line is not always accounted for in sufficient detail. To properly do this, we can pursue further our asymptotic approach that relies on the assumption that the
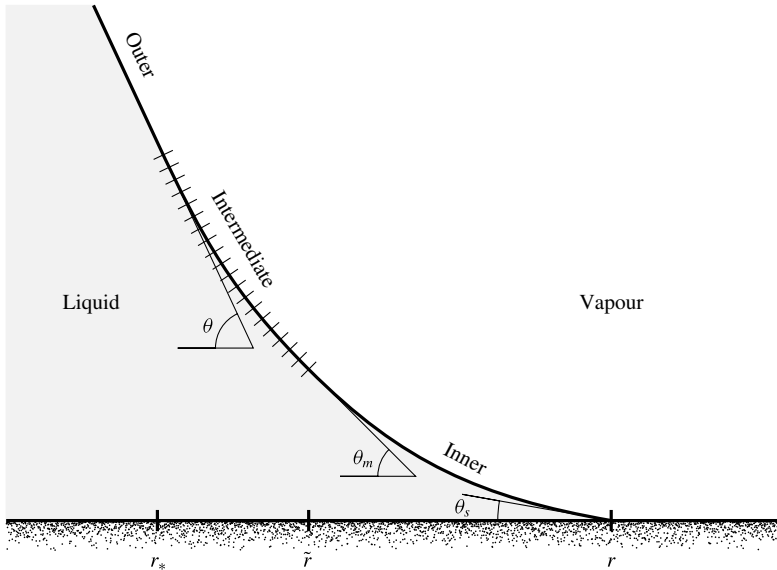
FIGURE 5. A schematic diagram showing the three regions in the vicinity of the contact line at $x = r$ (not drawn to scale), distinguishing between the apparent, macroscopic angle, θ, the microscopic, static angle, $\theta_s = 1$ (normalised to unity in our chosen non-dimensionalisation) and the evaporation-modified Young's angle, θ_m.

droplet size is much larger than $\mathcal{K}$ and λ. Ultimately, however, as the droplet volume diminishes, this formula will fail to describe the long-term behaviour of the volume, just as (3.21) will fail in this limit.

Unlike the matching carried out to obtain $\dot{r}$, to estimate $\dot{v}$ we need to consider all three regions, inner, intermediate and outer. This is particularly true if (2.20) is to be evaluated at the spreading stage, although, as alluded to earlier, $v(t)$ is not altered appreciably during this stage. Evaporation effects manifest themselves during the third stage, where $\theta \approx \theta_m$. As the transition to the evaporation stage occurs, the extent of the intermediate region shrinks and can be omitted altogether in the last two stages. However, in what follows we retain the presence of the intermediate region contributions for the sake of completeness.

Based on the above, we expect that all scales contribute to the net evaporative flux at leading order. To proceed, we split $\dot{v}$ into three parts, each consisting of an integral carried out in each region, namely

$$\dot{v} = q_1 + q_2 + q_3, \tag{3.24}$$

where

$$q_1 = -\int_{\tilde{r}}^{r} \frac{x\lambda E}{h + \lambda K} \, \mathrm{d}x, \quad q_2 = -\int_{r_*}^{\tilde{r}} \frac{x\lambda E}{h + \lambda K} \, \mathrm{d}x \quad \text{and} \quad q_3 = -\int_{0}^{r_*} \frac{x\lambda E}{h + \lambda K} \, \mathrm{d}x, \tag{3.25a-c}$$

with r_* and $\tilde{r}$ being the radii where the intermediate region matches within appropriate overlap regions with the solution in the outer and inner regions, respectively (see figure 5), i.e. such that $\tilde{\eta} = (r - \tilde{r})/\lambda \gg 1$ and $r - r_* \ll 1$, but, at the same time, we also

have $\dot{r} \ln \tilde{\eta} \ll 1$ and $\dot{r} \ln(r - r_*) \ll 1$. Based on these requirements for the asymptotics of $\tilde{r}$ and r_*, each integral in (3.25) is estimated by making use of the smallness of $\dot{r}$ and the appropriate asymptotic limits, retaining only the leading algebraic-order terms in λ.

The integral over the inner region is estimated using

$$q_1 = -\int_{\tilde{r}}^{r} \frac{x \lambda E}{h_{in} + \lambda K} \, \mathrm{d}x \sim -\int_{0}^{\tilde{\eta}} \frac{r \mathcal{E}}{\phi_0 + K} \, \mathrm{d}\eta, \qquad (3.26)$$

as $\lambda \to 0$, where we took $h_{in} = \lambda \phi_0(\eta)$, with $\eta = (r - x)/\lambda$ and ϕ_0 determined from (3.15). Using the asymptotics of ϕ_0 as $\eta \to \infty$ in the left-hand side of (3.15) and integrating, we find that (3.26) behaves like

$$q_1 \sim -\frac{r \mathcal{E}}{\theta_m} \ln(\tilde{\eta} \tilde{\beta} \theta_m \mathrm{e}^{-3/2}) \quad \text{as } \tilde{\eta} \to \infty, \qquad (3.27)$$

where $\tilde{\beta}$ is a parameter appearing in the next term of the asymptotics of $\partial_\eta \phi_0$ as a function of ϕ_0, namely

$$\partial_\eta \phi_0 \sim \theta_m - \frac{E}{2\theta_m^3 \phi_0} \ln(\phi_0 \tilde{\beta}) \quad \text{as } \phi_0 \to \infty \qquad (3.28)$$

and is determined using similar techniques as those discussed in appendix B. Had we merely used $h_{in} = \lambda \theta_m \eta$ in (3.26), which is the leading-order behaviour as we approach the intermediate region, we would have obtained

$$q_1 \sim -\frac{r \mathcal{E}}{\theta_m} \ln \frac{\theta_m \tilde{\eta}}{K} \quad \text{as } \tilde{\eta} \to \infty, \qquad (3.29)$$

which is equivalent to the inner-region contributions of (3.22) with $\theta = \theta_m$.

In figure 6 we show a few representative plots of $\tilde{\beta}$ for various values of E and K. In figure 6(a) we provide plots for $10^{-3} \leqslant E \leqslant 30$, to contrast the values of $\tilde{\beta}$ with $\mathrm{e}^{3/2}/K$ as a means to compare (3.27) and (3.29). It is readily seen that (3.29) gives a rough estimate for q_1 which works better for smaller values of E and larger values of K, i.e. for weaker evaporation effects. This is not surprising given that in this limit $\phi_0 \approx \eta$ with $\theta_m \approx 1$ (cf. appendix A) is no different from the simplified form used to obtain (3.29). In particular, it is interesting to note that the calculations presented in figure 6(a) suggest that $\tilde{\beta} \to \mathrm{e}^{3/2}/K$ as $E \to 0^+$.

To estimate q_2, perform a change of variable to the stretched coordinate η and consider to leading order as $\lambda \to 0$

$$q_2 \sim -\int_{\tilde{\eta}}^{\eta_*} \frac{\lambda^2 r E}{h_{int}} \, \mathrm{d}\eta, \qquad (3.30)$$

where $\eta_* = (r - r_*)/\lambda$ and h_{int} is the intermediate solution

$$h_{int} = \lambda \eta \left(\theta_m^3 + 3\dot{r} \ln \frac{\beta \eta}{\mathrm{e}} \right)^{1/3} \qquad (3.31)$$

as expressed in terms of the inner variable η. The derivation of (3.31) is nearly identical to the intermediate solution of Hocking (1983) for non-volatile droplets,
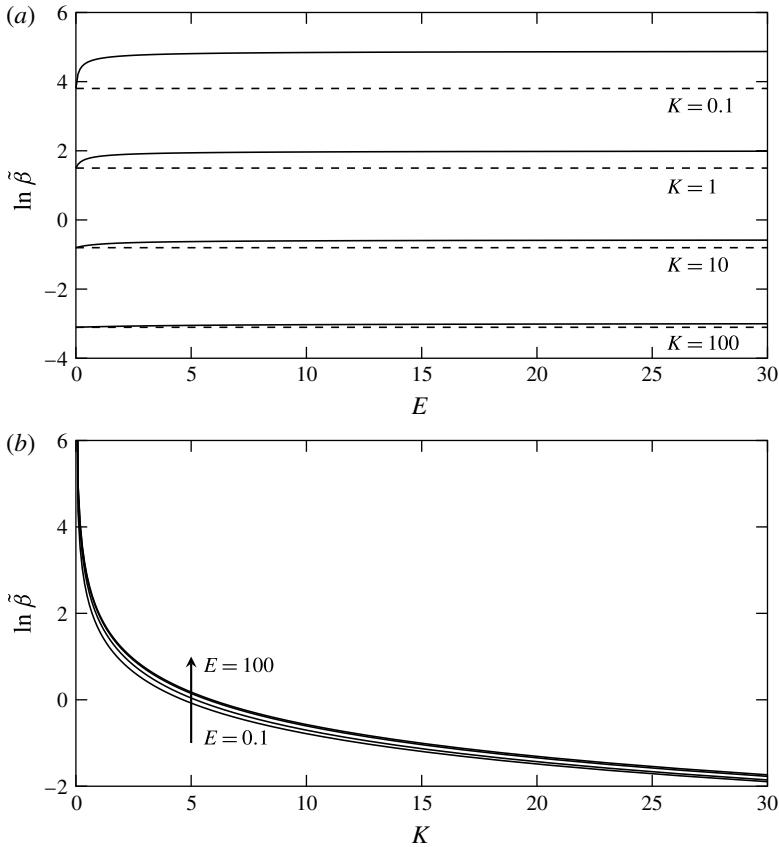
FIGURE 6. (*a*) Solid curves: plots of $\ln \tilde{\beta}$ as a function of E for various values of K and $0.001 \leqslant E \leqslant 30$; dashed curves: plots of $\ln(\mathrm{e}^{3/2}/K)$ corresponding to each of the values of K shown as solid curves, to compare (3.27) and (3.29). (*b*) Plots of $\ln \tilde{\beta}$ as a function of K for various values of E. The curves from bottom to top correspond to the values $E = 0.1$, 1, 10 and 100, respectively.

arguing, as in Saxton *et al.* (2016), that the evaporation term is negligible within the intermediate region and matching the solution with appropriate conditions at the far field of the inner region. In (3.30) we have neglected the kinetic resistance effects which is an acceptable approximation for $\mathcal{K} \ll 1$. Hence, we obtain

$$q_2 \sim -\frac{r\mathcal{E}}{2\dot{r}} \left[\left(\theta_m^3 + 3\dot{r} \ln \frac{\beta \eta_*}{\mathrm{e}} \right)^{2/3} - \left(\theta_m^3 + 3\dot{r} \ln \frac{\beta \tilde{\eta}}{\mathrm{e}} \right)^{2/3} \right]. \tag{3.32}$$

Next, we need to find the asymptotic behaviour of q_2 as we have both $\tilde{\eta} \to \infty$ and $r_* \to r$. Using (3.21) we modify the first term in the square brackets of (3.32) so that we can eventually take the limit $r_* \to r$. Hence we obtain

$$q_2 \sim -\frac{r\mathcal{E}}{2\dot{r}} \left\{ \left[\theta^3 + 3\dot{r} \ln \left(\frac{\mathrm{e}}{\delta} \frac{r - r_*}{r} \right) \right]^{2/3} - \left(\theta_m^3 + 3\dot{r} \ln \frac{\beta \tilde{\eta}}{\mathrm{e}} \right)^{2/3} \right\}, \tag{3.33}$$

noting that the limits $\tilde{\eta} \to \infty$ and $r_* \to r$ must be taken with the understanding that the $O(\dot{r})$ terms of the asymptotic expansions are still of higher order compared to the $O(1)$ terms. Hence, expanding into a series in $\dot{r}$ gives as $\lambda \to 0$

$$q_2 \sim -r\mathcal{E} \left\{ \frac{3(\theta + \theta_m)}{2(\theta^2 + \theta\theta_m + \theta_m^2)} \ln \frac{\beta\delta r}{\lambda e^2} + \frac{1}{\theta} \ln \left[\frac{e}{\delta} \left(1 - \frac{r_*}{r} \right) \right] - \frac{1}{\theta_m} \ln \frac{\beta\tilde{\eta}}{e} \right\}. \quad (3.34)$$

Lastly, to find the leading-order expression for the integral within the outer region, q_3, we neglect, just as in the intermediate region, kinetic resistance effects and consider

$$q_3 \sim - \int_0^{r_*} \frac{x\mathcal{E}}{h_0} \, \mathrm{d}x \quad (3.35)$$

as $\lambda \to 0$, where h_0 is the leading-order outer solution given by (3.4). Clearly the integrand has a logarithmic singularity as $r_* \to r$, since h_0 vanishes as $r_* \to r$. Hence, we can remove the singularity as $r_* \to r$ outside the integral by writing

$$q_3 \sim -\frac{\mathcal{E}}{\theta} \left\{ \int_0^r \left[\frac{x\sqrt{B}I_1(c)}{I_0(c) - I_0(x\sqrt{B})} - \frac{r}{r-x} \right] \mathrm{d}x - r \ln \left(1 - \frac{r_*}{r} \right) \right\} \quad (3.36)$$

as $r_* \to r$. In the limit $B \to 0$, equation (3.36) simplifies to

$$q_3 \sim \frac{r\mathcal{E}}{\theta} \ln \left[2 \left(1 - \frac{r_*}{r} \right) \right]. \quad (3.37)$$

Adding the contributions from (3.27), (3.34) and (3.36) cancels the singular terms involving $\ln \tilde{\eta}$ and $\ln(r - r_*)$ and we obtain an expression for $\dot{v}$ determined up to and including $O(\lambda)$ terms,

$$\dot{v} = -r\mathcal{E} \left\{ \frac{1}{\theta_m} \ln \frac{\tilde{\beta}\theta_m}{\beta e^{1/2}} + \frac{1}{\theta} \ln \frac{e}{\gamma\delta} + \frac{3(\theta + \theta_m)}{2(\theta^2 + \theta\theta_m + \theta_m^2)} \ln \frac{\beta\delta r}{\lambda e^2} \right\}, \quad (3.38)$$

where

$$\ln \gamma = \int_0^1 \left[\frac{1}{1-x} - \frac{xcI_1(c)}{I_0(c) - I_0(xc)} \right] \mathrm{d}x, \quad (3.39)$$

noting that $\gamma \to 2$ as $r\sqrt{B} \to 0$ (see figure 7 for plots of $\gamma(c)$ for pendant and sessile droplets). To compute γ for pendant droplets we take $c = r\sqrt{-B}$, replace the modified Bessel functions by Bessel functions and change the sign of the second term in (3.39). In the stages dominated by evaporation, where we can take $\theta \approx \theta_m$, equation (3.38) simplifies further to

$$\dot{v} = -\frac{\mathcal{E}r}{\theta} \ln \frac{\tilde{\beta}\theta r}{\gamma\lambda e^{3/2}}. \quad (3.40)$$

The arguments leading to the derivation of (3.38) reveal that it is able to capture the evolution of $v(t)$ both in the spreading and the evaporation stages as $\lambda \to 0$ and for $O(1)$ values for E, K and B. As it turns out, using the simpler expression (3.40) to simulate the full dynamics does not typically yield appreciably different results from using the more complete expression (3.38). This is mainly due to the fact that spreading takes place on a shorter time scale compared to the long evaporation stage during which $\theta \approx \theta_m$.
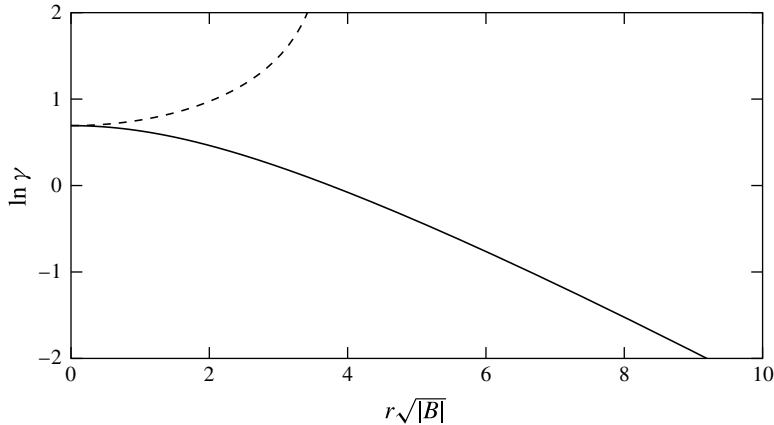
FIGURE 7. Dependence of $\ln \gamma$ on $r\sqrt{|B|}$ for a sessile ($B > 0$; solid curve) and a pendant ($B < 0$; dashed curve) droplet. As the droplet evaporates, $r \to 0$, the curves approach asymptotically the value of $\ln \gamma = \ln 2$, corresponding to the $B = 0$ case.

As already anticipated from our earlier discussion, equation (3.38) and, perhaps more transparently, equation (3.40) reveal that, in the distinguished limit under consideration, $\dot{v} = O(\lambda|\ln \lambda|)$ as $\lambda \to 0$. Comparing this scaling with the scaling $\dot{r} = O(1/|\ln \lambda|)$ as $\lambda \to 0$, which was deduced from (3.21), confirms *a posteriori* the assumptions underpinning the analysis of the second stage, namely that $\lambda \ll \dot{r} \ll 1$ and $\dot{v} \ll \dot{r}$. However it is clear that our analysis will break down when the argument of the logarithm in (3.40) tends to unity with $r \to r_c$, where

$$r_c = \frac{\gamma \lambda e^{3/2}}{\tilde{\beta} \theta_m} = O(\mathcal{K}), \tag{3.41}$$

i.e. when the size of the droplet becomes comparable to the kinetic length scale. When this happens, equation (3.40) incorrectly predicts that $\dot{v} \to 0$ with $v \neq 0$. This indicates that $\mathcal{K}$ can no longer be assumed to be smaller than the droplet size which invalidates the assumptions put forth for our analysis to hold.

The derivation of an evolution equation for $v(t)$ concludes the asymptotic analysis we have undertaken. Although we concede that the arguments we presented above are centred around the spreading time scale, we did not deem necessary a separate treatment of the evaporation stage to produce a composite expansion valid across both stages, as done, for example in the analysis of Saxton *et al.* (2016). Later on, we will offer some heuristic arguments as to why doing so is acceptable (see § 4.2), but, more importantly, throughout the following section we will provide rather compelling numerical evidence from over one hundred simulations of the governing partial differential equation, which are found to be in excellent agreement with the predictions of the equations (3.21) and (3.38) obtained from matching.

4. Numerical results

In this section, the findings of our analysis are scrutinised against the solutions to the full problem, offering the appropriate commentary to elucidate the effects of the various parameters of the problem. In what follows, the full problem refers to
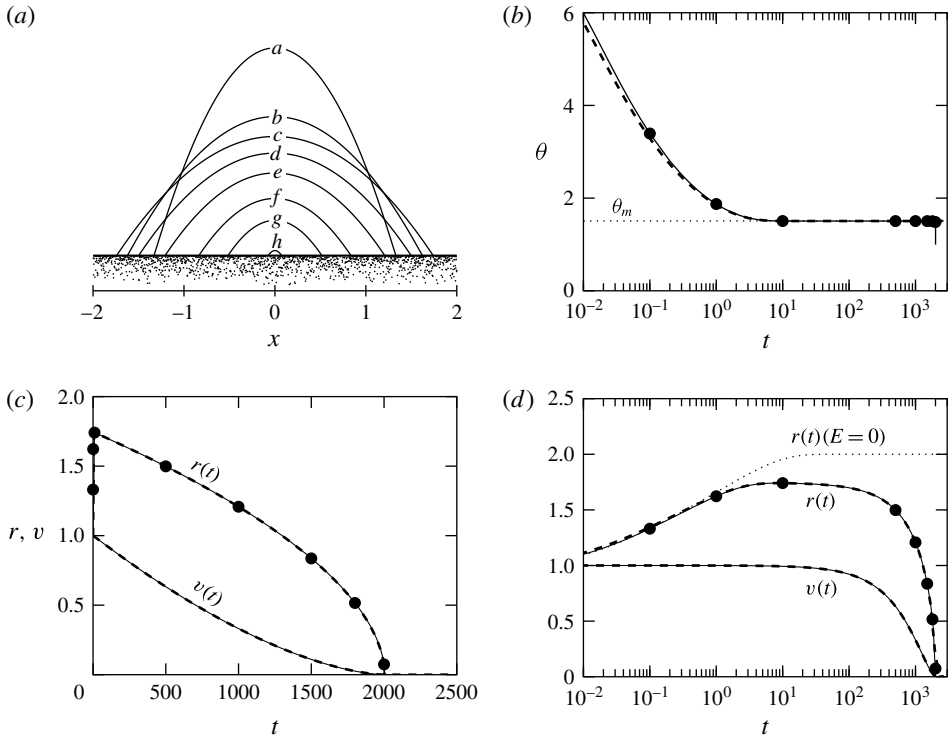
FIGURE 8. Evaporating droplet with $\lambda = 2 \times 10^{-5}$, $E = 4$, $K = 14$, $B = 0$ and $v(0) = r(0) = 1$. (*a*) Droplet profiles at different times obtained from the full problem; curves '*a*'–'*h*' correspond to the profiles when $t = 0.1$, 1, 10, 500, 1000, 1500, 1800 and 2000, respectively. In (*b*–*d*), the solid and dashed curves correspond to the solutions of the full and reduced problems, respectively (in most plots the curves cannot be distinguished from each other); the solid circles correspond, left to right in each plot, to data taken from the profiles '*a*'–'*h*', respectively. (*b*) Evolution of the apparent contact angle, equation (3.6*b*), demonstrating the transition to θ_m (dotted line). (*c,d*) Evolution of r and v in linear and logarithmic time scales, respectively. The dotted curve in (*d*) shows the evolution of r in the non-volatile case for comparison.

the governing partial differential equation, equation (2.14), subject to the boundary conditions (2.18) and the appropriate initial condition (see appendix C), whereas the reduced problem refers to the system of differential equations obtained from the asymptotic analysis, equations (3.21) and (3.38), and its corresponding initial conditions. The numerical methods used to solve both problems are briefly outlined in appendix C. All parameters used are loosely based on the parameters used for some of the liquids discussed in § 2, because we are after the qualitative features of the dynamics and reasonably realistic parameter values are generally sufficient for this purpose.

4.1. *The four-stage dynamics*

Figure 8 shows a typical calculation which is performed for parameters that are close to the values for water reported in § 2. We see that the solutions of the full (solid curves) and reduced problems (dashed curves) are visually indistinguishable and

the solutions are on top of each other; there are some barely noticeable differences at early times (see, e.g. figure 8b), which are solely attributed to our choice of ϵ. Indeed, if we repeat the calculation with a much smaller value of ϵ, the dynamics is indistinguishable throughout. We should also note that using the simpler expression for $\dot{v}$, equation (3.23), instead of the more rigorously obtained (3.38) the agreement between the full and reduced problems degrades and the solutions no longer exhibit such excellent agreement, particularly during the late stages of the dynamics (see also § 4.3).

From figure 8 we see that the contact line advances initially up to $t = O(10) = O(1/|\ln\lambda|)$ and then gradually recedes due to evaporation, with the apparent contact angle, defined by (3.6b), being close to the evaporation-modified Young's angle (see figure 8b), as expected from our analysis. Looking at the various plots in figure 8, we can identify the four stages for the evaporation dynamics of the contact line, anticipated earlier in the discussion, at the beginning of § 3. The first stage, is typically very brief and corresponds to the relaxation of the droplet shape in the bulk to the leading-order outer solution (in this calculation the first stage lasts approximately up to $t = O(0.1)$). In the second stage, the dynamics is driven primarily by (3.21) with $v(t) \approx v(0)$. This is evidenced in figure 8(d), where we show for comparison the evolution of the droplet radius in the non-volatile case. Here we see good agreement with the non-volatile case up to $t = O(1)$, but the agreement degrades when θ^3 becomes of the same order of magnitude as θ_m^3, which, interestingly, occurs long before the volume changes become appreciable. Due to the brief duration of the first two stages, the volume of the droplet hardly changes (see, e.g. the droplet profiles 'a'–'c' in figure 8a and the plots of r and v against a logarithmic time scale in figure 8d).

The distinguishing characteristic of the third stage is that the apparent contact angle remains close to θ_m. During this stage, evaporation effects dominate the dynamics and most of the liquid of the droplet evaporates into the saturated atmosphere (see, e.g. the droplet profiles 'd'–'h' in figure 8a and the plots of r and v against a linear time scale in figure 8c). At the fourth stage, the droplet becomes too small and all assumptions upon which our analysis is based no longer hold. Hence, this stage is not captured by the reduced model; the computations of the full problem suggest that during this final stage θ decreases abruptly below θ_m (see figure 8b). These final moments of the droplet's lifetime are admittedly rather difficult to resolve with high accuracy due to the computation being prone to round-off errors and the aforementioned difficulties associated with the stiffness of the full problem. Nevertheless, it is clear that this stage will be rather short in duration and is thus deemed of lesser importance in our discussion.

In a second example, we test the limits of applicability of our analysis by considering the case of an FC-72-like droplet discussed in § 2. More specifically, if we consider the case when $\Delta\Theta = 10$ K, $\vartheta_s = 4°$, $d = 2.2$ mm, while all other parameters are kept unchanged, we have approximately the following parameters, $E = 9800$ ($\mathcal{E} = 0.20$), $K = 14$ and $\lambda = 2 \times 10^{-5}$. This is a rather extreme scenario given that the value of $\mathcal{E}$ is comparatively large and perhaps beyond the regime of applicability of our asymptotic theory. Yet, as figure 9 shows, our theory still applies and accurately predicts the dynamic behaviour of the full problem. Even in this case we have nearly indistinguishable dynamics throughout. However, here we see that the droplet recedes from the outset due to the evaporation-modified Young's angle being larger than the initial apparent contact angle (as also remarked by Todorova *et al.* 2012). This calculation is also an example which illustrates that the distinction and
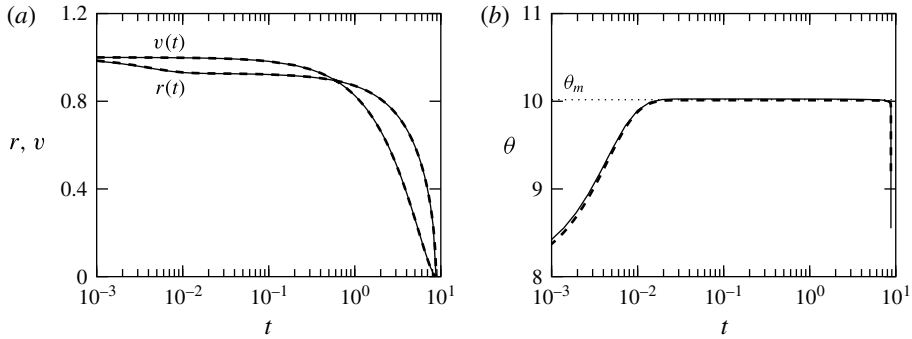
FIGURE 9. Evaporating droplet with $E = 9800$, $K = 14$, $B = 0$, $\lambda = 2 \times 10^{-5}$, $\epsilon = 10^{-2}$ and $v(0) = r(0) = 1$. (*a*) Evolution of the droplet radius and volume. (*b*) Evolution of the apparent contact angle, equation (3.6*b*). In (*a*,*b*) the solutions to both the full (solid curves) and the reduced problems (dashed curves) are virtually indistinguishable.

duration of the previously discussed stages are strongly dependent on the parameters of the problem. The estimated evaporation time in this case is $t_* \approx 8.8$. Based on the parameters of the problem, we can conclude that a droplet of volume 4.7 µl would evaporate completely within 10 s, a figure which is in the right ballpark based on the discussion in the work of Raj *et al.* (2012).

4.2. *The evaporation stage*

From the results presented above, we saw that (3.21) and (3.38) are able to adequately describe the dynamics throughout. We also saw that the droplet evaporates completely in finite time after a comparatively long third stage, which is the stage during which the apparent contact angle is roughly equal to the evaporation-modified Young's angle. Thus, if we simply take $\theta \approx \theta_m$, equation (3.21) gives $\dot{r} \approx 0$, i.e. the contact line velocity is very small and the contact line motion is slaved to the slow process of evaporation, so that $\dot{r} \approx 2\dot{v}/(3\theta_m^{1/3} v^{2/3})$ (when $B = 0$). This means that at the onset of the third stage, where $v = O(1)$, both $\dot{r}$ and $\dot{v}$ are of the same order and hence $\dot{r}$ ceases to be the greatest smallness parameter, and, self-consistently, one can neglect its active role when evaporative effects dominate. However, as $v \to 0^+$, it follows that, just as in the second stage, we have that $\dot{r} \gg \dot{v}$. This means that (3.21), which arises from the quasi-static analysis of the second stage may become relevant again. Thus we can reasonably expect that both the reduced problem, equations (3.21) and (3.40), and the modified problem in which (3.40) is solved together with $\theta = \theta_m$ (see also Saxton *et al.* 2016) will yield comparable results. Undertaking a more rigorous approach to justify this argument is likely to be rather unwieldy, so instead we resorted to making comparisons of the solutions of the reduced and modified problems with the full problem when $B = 0$ with $r(0) = 2/\theta_m^{1/3}$ and $v(0) = 1$ for various choices of E and K. The particular choice for $r(0)$ was made to ensure that the droplet does not undergo a spreading stage. For all cases considered, the reduced problem was visually indistinguishable from the full problem, whereas with the modified problem there were small differences which became more noticeable as $r \to 0^+$. This provided us with sufficient numerical evidence that the validity of (3.21) can be extended into the evaporation stage as well, as it is able to capture the transition of $\theta \to \theta_m$ and dynamics of the evaporation stage as $v \to 0^+$, provided that $r \gg \lambda$.

On the other hand, by replacing (3.21) with $\theta = \theta_m$ in the reduced problem, we can decouple the system of equations for $r(t)$ and $v(t)$ so that we can utilise just the equation for $\dot{v}$. Since the droplet loses an order unity of its volume during the slow evaporation stage, this ultimately allows us to obtain an estimate of the time it takes a droplet of initial volume $v(0) = v_0$ to evaporate completely when $B = 0$. The evaporation time, t_*, can be computed from (3.40) and using $r = 2v^{1/3}\theta_m^{-1/3}$, namely

$$t_* = \frac{\theta_m^{4/3}}{2\mathcal{E}} \int_0^{v_0} \frac{\mathrm{d}v}{v^{1/3} \ln \dfrac{\tilde{\beta}\theta_m^{2/3}v^{1/3}}{\lambda \mathrm{e}^{3/2}}}. \tag{4.1}$$

It is important to note that since (3.40) does not allow the volume to vanish completely, the integral for estimating t_* only exists in the Cauchy principal value sense and as such is given above. Similar considerations can be followed to obtain t_* when $B \neq 0$, but the integral expression is cast with the radius being the variable of integration. Unlike the case with $B \neq 0$, equation (4.1) can be evaluated analytically to obtain

$$t_* = \frac{3\lambda^2 \mathrm{e}^3}{2\mathcal{E}\tilde{\beta}^2} \mathrm{Ei}\left(\ln \frac{v_0^{2/3}\tilde{\beta}^2\theta_m^{4/3}}{\lambda^2 \mathrm{e}^3} \right), \tag{4.2}$$

where $\mathrm{Ei}(x)$ is the exponential integral, defined as

$$\mathrm{Ei}(x) = -\int_{-x}^{\infty} \frac{\mathrm{e}^{-y}}{y} \, \mathrm{d}y \tag{4.3}$$

for $x > 0$. Using the large-argument expansion $\mathrm{Ei}(x) = \mathrm{e}^x/(x-1) + O(\mathrm{e}^x x^{-3})$, we can write (4.2) as

$$t_* = \frac{3}{4\mathcal{E}} \frac{v_0^{2/3}\theta_m^{4/3}}{\ln \dfrac{\tilde{\beta}v_0^{1/3}\theta_m^{2/3}}{\lambda \mathrm{e}^2}}. \tag{4.4}$$

Although $\mathcal{K}$ does not appear explicitly in (4.4), it is clear from our earlier discussion that $\mathcal{K}$ together with $\mathcal{E}$ and λ influence the values of both θ_m and $\tilde{\beta}$ which appear in (4.4) above.

Figure 10 shows the dependence of t_* on the initial droplet volume for two different sets of parameters. The values of t_* obtained from solutions to the full problem are in excellent agreement with the values predicted with (4.4). Unlike the typical scaling $t_* \sim v_0^{2/3}$, which can be deduced by simple arguments, e.g. by assuming the integral evaporation flux to be proportional to the droplet radius, in this set of parameters we have found better agreement with the scaling $t_* \sim v_0^{0.63}$ for both sets of calculations (note that other exponents can be obtained for different values of the system parameters). This result highlights the importance of the presence of the logarithmic terms in (4.4) in modulating the power law. An important consequence of the calculation presented above is that the evolution of $v(t)$ and $r(t)$ during the evaporation stage can be approximately predicted using the implicit formulae

$$t_* - t = \frac{3}{4\mathcal{E}} \frac{v^{2/3}\theta_m^{4/3}}{\ln \dfrac{\tilde{\beta}v^{1/3}\theta_m^{2/3}}{\lambda \mathrm{e}^2}} \quad \text{and} \quad t_* - t = \frac{3}{16\mathcal{E}} \frac{r^2\theta_m^2}{\ln \dfrac{\tilde{\beta}r\theta_m}{2\lambda \mathrm{e}^2}}. \tag{4.5a,b}$$
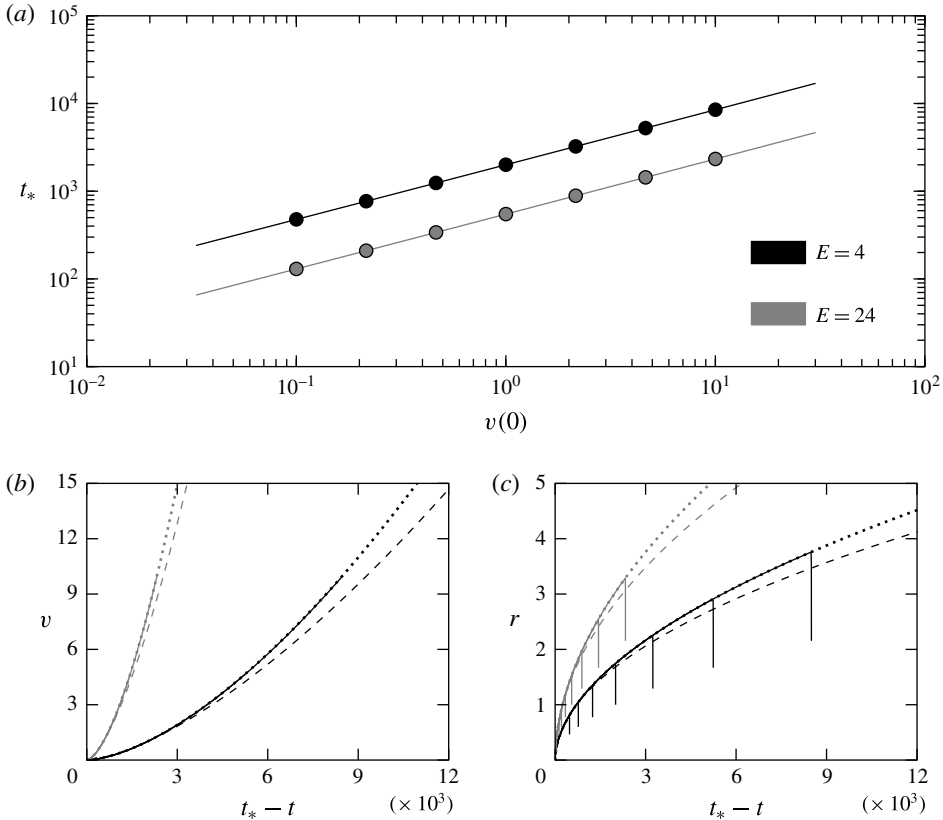
FIGURE 10. (a) Evaporation times for droplets with $K = 14$, $B = 0$, $\lambda = 2 \times 10^{-5}$ and $v(0) = 10^{n/3}$, $r(0) = 2\theta_m^{-1/3}[v(0)]^{1/3}$ for $n = 0, \pm 1, \pm 2, \pm 3$, when $E = 4$ (black circles) and $E = 24$ (grey circles), as predicted by the solution to the full problem. The solid curves correspond to the predictions of (4.4) for each set of parameters. (b,c) Plots of v and r as functions of $t_* - t$ for each solution to the full problem from (a), respectively. For each set of parameters (grey curves for $E = 24$ and black curves for $E = 4$), the data ultimately collapse onto the same dotted curve, which corresponds to the theoretical prediction of (4.5); the dashed curves in (b) and (c) correspond to the classical power laws $v \sim (t_* - t)^{3/2}$ and $r \sim (t_* - t)^{1/2}$, respectively.

The above predictions are readily verified in figures 10(b) and 10(c), where we plot v and r, respectively, as functions of $t_* - t$ for all 14 solutions of the full problem (solid curves), which were performed in preparation of figure 10(a). Looking at figure 10(b), all data from the solutions to the full problem collapse onto two (dotted) curves, corresponding to the theoretical result, (4.5a), for the two different sets of parameters under consideration. The same happens when we plot r as a function of $t_* - t$ (see figure 10c), apart from the brief initial transients in the first two stages of the dynamics, which appear as nearly vertical lines in the plot. For comparison, we included in figure 10(b,c) the simple power-law scalings, $v \sim (t_* - t)^{3/2}$ and $r \sim \sqrt{t_* - t}$, respectively, to demonstrate that they do not always predict the behaviour of the system accurately. In fact better fit to the data with the radius is provided by power laws with an exponent of approximately 0.53, i.e. slightly larger than $1/2$. Interestingly, this is in qualitative agreement with what has been reported in the
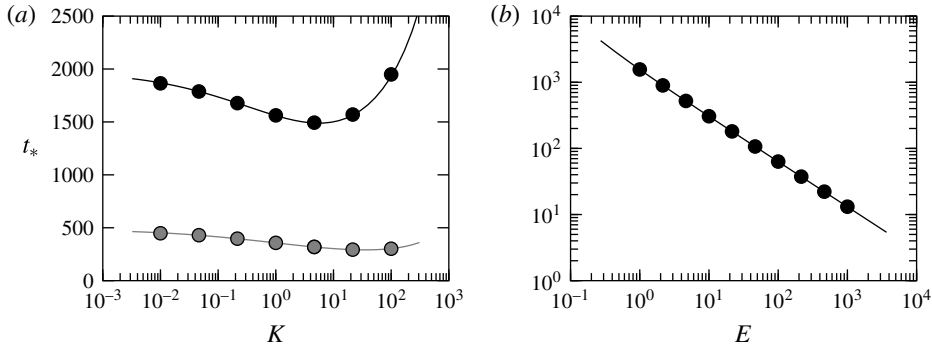
FIGURE 11. (*a*) Influence of K on the evaporation time, for droplets with $\lambda = 10^{-4}$, $B = 0$, $v(0) = r(0) = 1$ for two different values of E, namely $E = 1$ (black) and $E = 8$ (grey). The solid curves correspond to the theoretical prediction, equation (4.4); the circles represent the results obtained by solving the full problem when $K = 10^{-2n/3}$, $n = 0, \pm 1, \pm 2, \pm 3$. (*b*) Influence of E on the evaporation time, for droplets with $\lambda = 10^{-4}$, $B = 0$, $K = v(0) = r(0) = 1$. The solid curve corresponds to (4.4); the circles to solutions of the full problem for $E = 10^{n/3}$, $n = 0, 1, 2, \ldots, 9$.

literature for diffusion-limited evaporation of water droplets (Cazabat & Guéna 2010). However, as will be discussed later, our model predicts such apparent exponents to be always larger than $1/2$, which does not match experiments with other liquids. This is not surprising given the different evaporation regime (limited mostly by heat transfer) considered here.

In figure 11(*a*) we show typical plots demonstrating the dependence of t_* on K. We find that t_* increases with K provided that K is large enough. This dependence, however, is not monotonic and there exists a moderate value of K for which t_* attains a minimum. This can be attributed to the different mechanisms that operate at disparate values of K. The increase of t_* for large values of K is to be expected, since the evaporative flux diminishes as K increases. For small K, decreasing K towards 0 increases θ_m (and the apparent contact angle as a result), which in turn decreases the evaporative flux, given that the droplet becomes thicker with a smaller evaporation surface and a smaller contact area with the substrate. Nevertheless, these effects are less dramatic for larger values of E, as the comparison of the two sets of calculations in figure 11(*a*) reveals. The dependence of t_* on E is more straightforward to describe, since, as expected, we always have a monotonic decrease of the evaporation time with E (see figure 11*b*). We should note that although E appears explicitly at the denominator of t_*, see (4.4), θ_m and $\tilde{\beta}$ also depend on E, giving rise to non-trivial power-law dependencies (best fit to the data in figure 11*b* was achieved with $t_* \sim E^{-0.69}$).

4.3. *The large-K limit*

The large-K limit can be of relevance if f_a is rather small for the reasons outlined in § 2. For example, some experimental studies with water reported values of $O(10^{-3})$ for f_a (see Marek & Straub 2001, and the references therein). In this limit, we expect that the evolution of $v(t)$ will not be well described by (3.38) because the analysis ceases to work for relatively large radii, see (3.41).
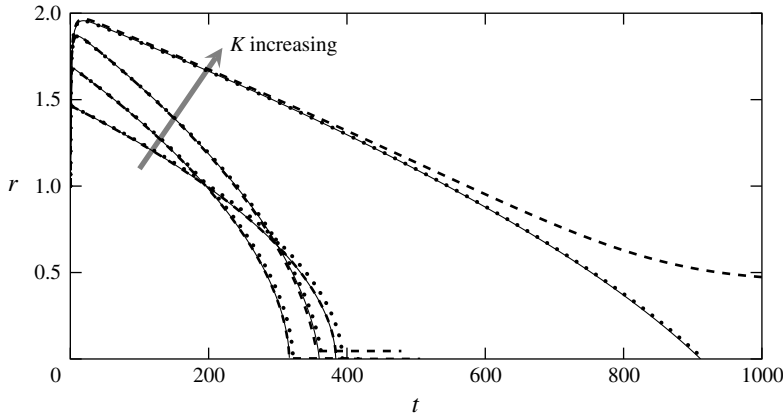
FIGURE 12. Comparison of the asymptotic predictions with the solution to the full problem for the evolution of $r(t)$ (solid curves) with $\lambda = 2 \times 10^{-5}$, $E = 40$, $B = 0$, $v(0) = r(0) = 1$ and for $K = 14$, 140, 1400 and 14 000. The dashed curves show solutions to (3.21) with (3.38); the dotted curves show the solutions to (3.21) with (3.23). As K increases, the agreement of the dashed curves with the full solution degrades; the opposite happens with the dotted curves.

At the same time, one can also infer from figure 6(*a*) and the discussion about q_1 that simply approximating the inner region as a wedge of slope θ_m suffices to capture well the inner-region contributions to $\dot{v}$. This, in turn, means that utilising the simpler expression for $\dot{v}$, equation (3.22), or, when $B = 0$, the exact expression (3.23), will provide a better approximation for $\dot{v}$, noting that it does not suffer from the cutoff radius limitation of (3.38). By following similar arguments as in the derivation of (4.4) we obtain an estimate for t_* that pertains in this limit, namely

$$t_* = \frac{3 v_0^{2/3} \theta_m^{4/3}}{4 \mathcal{E} \ln \dfrac{v_0^{1/3} \theta_m^{2/3}}{\mathcal{K} \mathrm{e}^{1/2}}}, \qquad (4.6)$$

where $\mathcal{K}$ appears explicitly, unlike (4.4) where the dependence on K is implicit.

Sample computations with large values of K are shown in figure 12 for water-like parameters (see also figure 8). The evolution of $v(t)$ is not shown here because the differences are more subtle compared to those seen in the evolution of $r(t)$. Here we compare the solutions to the full problem (solid curves) and solutions to the reduced problems using (3.21) either with (3.38) (dashed curves) or with (3.23) (dotted curves) for various values of K. We demonstrate that indeed using (3.38) is not appropriate for the larger values of K because r_c becomes unacceptably large. In contrast, equation (3.23) appears to perform well throughout, albeit with less favourable agreement for moderately large values of K, particularly as $t \to t_*$ (see, e.g. the calculation when $K = 14$). Note also that the non-monotonic variation of t_* with K (the simulation with $K = 14$ requires a longer time for the droplet to evaporate compared to $K = 140$ and $K = 1400$) is consistent with what has been observed in figure 11(*a*).
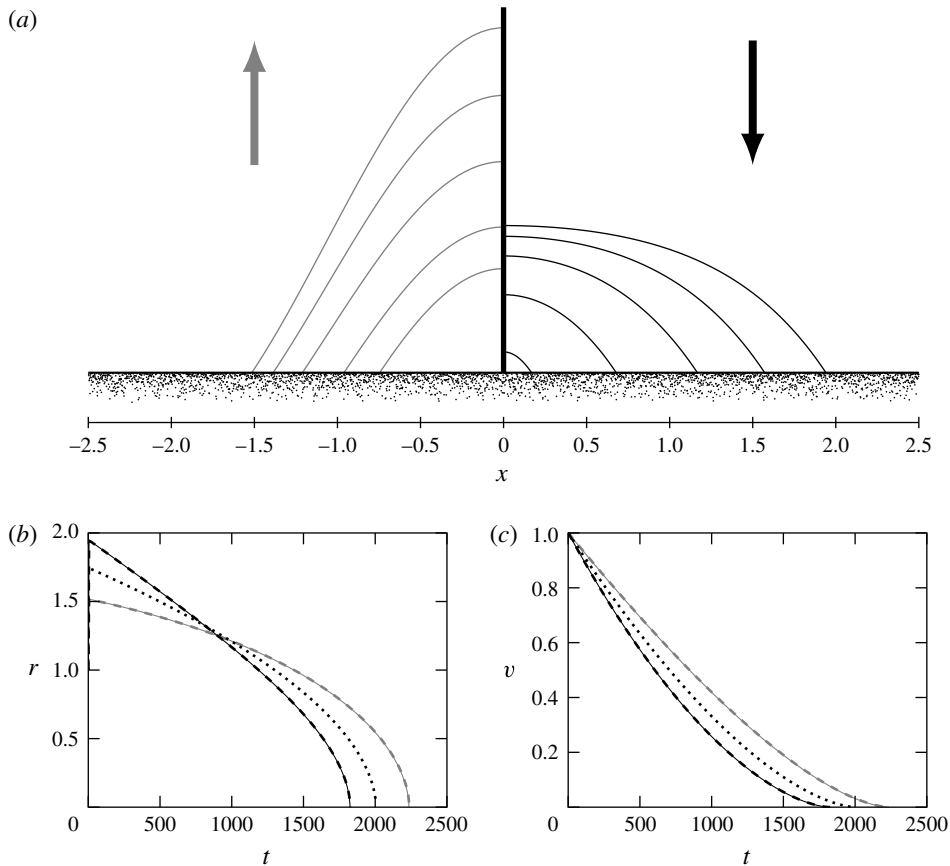
FIGURE 13. Comparison of pendant (grey curves) and sessile (black curves) droplet dynamics when $|B| = 3$; the rest of the parameters are as in figure 8. (*a*) Snapshots of pendant (left) and sessile (right) droplets at different times. Top to bottom profiles correspond to $t = 10, 500, 1000, 1500$ and 1800, respectively; arrows indicate the direction of gravity. (*b,c*) Evolution of the droplet radius and volume, respectively. Solid curves show the solutions to the full problem; the solutions to the reduced problem (dashed curves) are indistinguishable from those to the full problem. For comparison, the solution when $B = 0$ is also shown (dotted curves).

4.4. *The influence of gravity; pendant droplets*

As previously mentioned, the effect of gravity diminishes as the droplet shrinks in size due to evaporation. Although the qualitative features of the dynamics remains unaltered, a number of important observations can be made in relation to the effect of gravity on the evaporation time. Figure 13 summarises the results of two calculations using the same parameters and initial condition as in figure 8, but with non-zero Bond number. More specifically, we study the case when $B = 3$ (sessile droplet) and $B = -3$ (pendant droplet) and the results are contrasted with the calculation of figure 8, where $B = 0$. First, we note the excellent agreement of our theory with the solutions to the full problems, confirming that our analysis is applicable when $B \neq 0$ as well. Second, we see from these plots that the sessile droplet evaporates faster than the pendant one, with the droplet in the zero-gravity case completely evaporating at some instant in
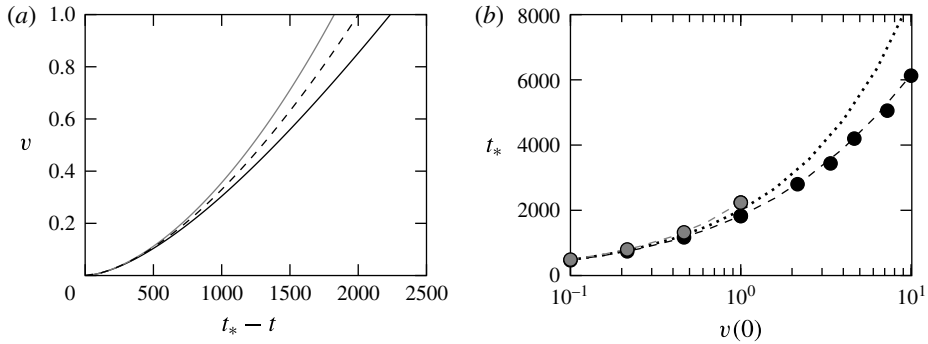
FIGURE 14. (*a*) Plot of the evolution of the volume shown in figure 13(*c*) as a function of $t_* - t$. (*b*) Plot of the evaporation time, t_*, as a function of the initial volume when $B = 3$ (black circles) and $B = -3$ (grey circles). The rest of the parameters are as in figure 13. The circles correspond to data extracted by solving the appropriate full problems. The dotted curve corresponds to the theoretical estimate, equation (4.4); the dashed curves in (*b*) are numerically computed evaporation times, using techniques which were discussed in § 4.2.

time between the two. The reason for the enhanced evaporation for the sessile droplet can be readily deduced in figure 13(*a*), where we see that gravity flattens a sessile droplet, which, apart from increasing the contact area, also boosts the evaporation rate density, see (2.10). This ultimately increases the evaporation flux, particularly at early times, when gravity manifests itself more strongly. Exactly the opposite happens when considering pendant droplets due to the fattening of the droplet near its axis of symmetry (see left-hand side of figure 13*a*).

If the evolution for the volume shown in figure 13(*c*) is plotted as a function of $t_* - t$ (see figure 14*a*) we see that for gravitational effects to be negligible, namely for the curves to approach the dashed curve corresponding to the zero gravity case, a rather significant amount of time must elapse until the volume of the droplet becomes sufficiently small. Indeed, a similar observation can be made if we plot the evaporation time as a function of the initial volume when $B = \pm 3$ (see figure 14*b*). For smaller volumes, the estimate given by (4.4), the dotted curve, is reasonable. However, for larger sessile droplets, there is a significant deviation of the evaporation time from the value predicted by (4.4). This deviation can be estimated by numerical means by following the same principles as in § 4.2 which were invoked in estimating t_* when $B = 0$ – see the dashed curves in figure 14(*b*). We should note here that for pendant droplets only four data points were collected by solving the full problem for volumes between 0.1 and 1 due to the previously mentioned critical value of $c \approx 3.83$, beyond which pendant droplets cannot be suspended from the substrate and droplet detachment/breakup may occur.

4.5. *The influence of slip*

From the preceding discussion, we saw that λ can influence the parameters of the inner-region asymptotics appearing in (3.21) and (3.38), namely θ_m, β and $\tilde{\beta}$ if we keep the other parameters of the system fixed (i.e. for fixed $\mathcal{E}$ and $\mathcal{K}$). For example, in figure 15 we present the results of two computations where we keep all system parameters the same apart from the values of λ. We see that when $\lambda = 10^{-3}$, the
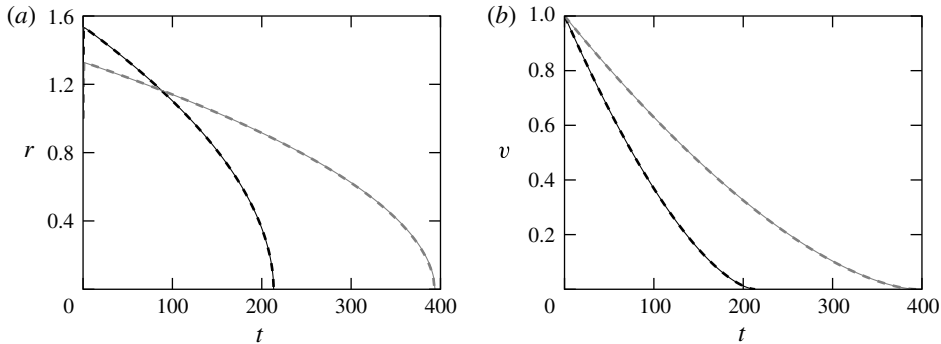
FIGURE 15. (*a*) and (*b*) depict the evolution of the droplet radius and volume, respectively for two disparate values of the slip length, λ, 10^{-5} (grey curves) and 10^{-3} (black curves). The rest of the parameters are $\mathcal{E} = 10^{-3}$, $\mathcal{K} = 10^{-4}$, $B = 0$ with $v(0) = r(0) = 1$. The solutions to the full problems are shown as solid curves and are indistinguishable from those of the reduced problems (plotted as dashed curves).
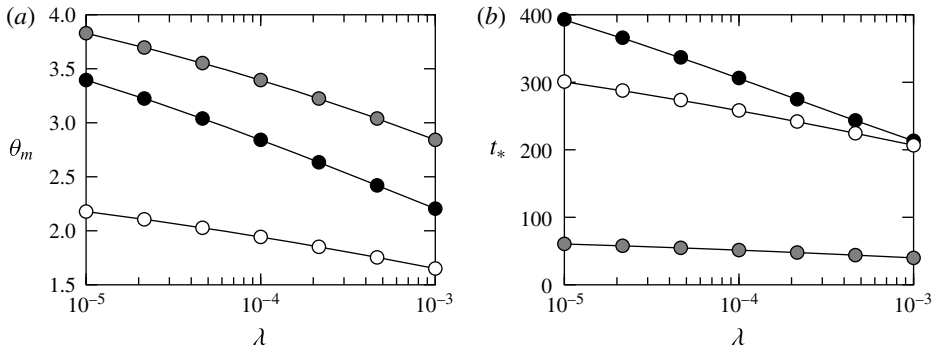

FIGURE 16. (*a*) Dependence of θ_m on λ and for three sets of pairs of values $(\mathcal{E}, \mathcal{K})$: $(10^{-3}, 10^{-4})$ – curves marked by black circles; $(10^{-3}, 10^{-3})$ – curves marked by white circles; $(10^{-2}, 10^{-3})$ – curves marked by grey circles. (*b*) Dependence of t_* on λ for the same set of parameters as in (*a*), $B = 0$ and $v(0) = r(0) = 1$. The circles correspond to values of t_* obtained from the full problem; the solid curves correspond to the estimate given by (4.4).

droplet spreads more and, as a consequence of the flattening of the droplet, total evaporation occurs faster, nearly twice as fast compared to the case when $\lambda = 10^{-5}$. Figure 16(*a*) shows that θ_m decreases as λ increases for fixed $\mathcal{E}$ and $\mathcal{K}$, thus explaining why in the computations of figure 15 the droplet with the larger λ spreads to a larger radius before entering the evaporation stage. Lastly, figure 16(*b*) shows solutions of the full problem (circles) compared with the predictions of (4.4) (solid curves). In all computations considered, we see that t_* decreases nearly linearly as $\ln \lambda$ increases with a slope which depends on the other parameters of the system, although for comparatively larger values of $\mathcal{E}$ the dependence of t_* on λ becomes weaker.

4.6. *The influence of substrate wettability*

The wettability of a substrate is characterised by the value of Young's equilibrium contact angle, ϑ_s. It is thus of interest to explore its effect on the dynamics and, more

specifically on the evaporation time. One may naturally expect that a lower value for ϑ_s would cause the droplet to spread more, thus increasing its contact area with the wall, so that, just as gravity, shorter evaporation times would be observed.

To demonstrate this, consider a calculation of a fluid with parameters $E = 0.125$, $K = 14$, $\lambda = 2 \times 10^{-5}$ and a Young's angle of $\vartheta_s = 20°$, subject to the initial condition $r(0) = 1.5$ and $v(0) = 1$. This set of parameters, denoted as set A, corresponds to parameter values which are close to those of FC-72. This calculation is repeated with all physical parameters kept the same, apart from ϑ_s which is taken to be $\vartheta_s = 10°$ (set B). To maintain the same scaling for the radius and keep the same dimensional initial volume as in set A, E must be increased by 16 times, whereas $v(0)$ and λ must undergo a twofold increase, whilst the rest are kept the same (hence, $E = 2$, $v(0) = 2$ and $\lambda = 4 \times 10^{-5}$ for set B). This is because E scales with ϑ_s^{-4}, whereas λ and V_0 scale with ϑ_s^{-1} if the characteristic length scale, d, is to be kept constant. Hence, decreasing ϑ_s further to $5°$ (set C), we need to take $E = 32$, $\lambda = 8 \times 10^{-5}$ and $v(0) = 4$, with the remaining parameters kept the same as in set A. The results of these calculations are shown in figure 17(a). Since time scales differently across the three set of parameters (left-hand side of figure 17a), a proper comparison of the dynamics in the three cases would be made by matching the time scales of each set. Hence, on the right-hand side of figure 17(a), we match the time scales of the sets A and C to that of set B and we see that the actual evaporation time is approximately 76 % higher in set A and 12 % lower in set C compared to the evaporation time of set B.

By increasing the values of E in all three sets of parameters by 12 times and producing their corresponding plots in figure 17(b), we find that the curves for sets B and C nearly collapse on top of each other when time is rescaled, with the dimensional evaporation time in set B differing from those of sets A and C by about 17 % and 1 %, respectively (right-hand side of figure 17b). A further increase in the values of E in all three sets of parameters of figure 17(a) by 144 times (i.e. 12 times higher compared to the calculations of figure 17b) yields the plots shown in figure 17(c). We readily observe that all curves nearly collapse on top of each other when time is rescaled appropriately as in panels (a) and (b) (see right-hand side of figure 17c). In this case, we find that the dimensional evaporation time in set B differs from those of A and C by approximately 2 % and 0.1 %, respectively.

From these calculations, we see that for small values of E there is a clear dependence of the dynamics on the value of ϑ_s, which aligns with the expectation that lower values for ϑ_s yield shorter evaporation times. However, we have also seen that for sufficiently large values of E the dependence of the evaporation time on ϑ_s diminishes. This can be rationalised by using (4.4) to cast the dimensional evaporation time in terms of the parameters of the problem as

$$\frac{3\rho L V_0^{2/3} \vartheta_m^{4/3}}{4k\Delta\Theta(2\pi)^{2/3}} \left[\ln \frac{\tilde{\beta} V_0^{1/3} \vartheta_m^{2/3}}{3be^2(2\pi)^{1/3}} \right]^{-1}, \tag{4.7}$$

where V_0 is the initial dimensional droplet volume. First, we note that ϑ_s does not appear explicitly in the expression above. The presence of ϑ_s is implicit, however, due to its influence on ϑ_m. At the same time, we have seen in §3.1.2 that this dependence diminishes in the strong evaporation limit ($E \gg 1$), which allows us to conclude that under such conditions the evaporation time becomes practically independent of the wetting properties of the substrate, which effectively corresponds to the completely
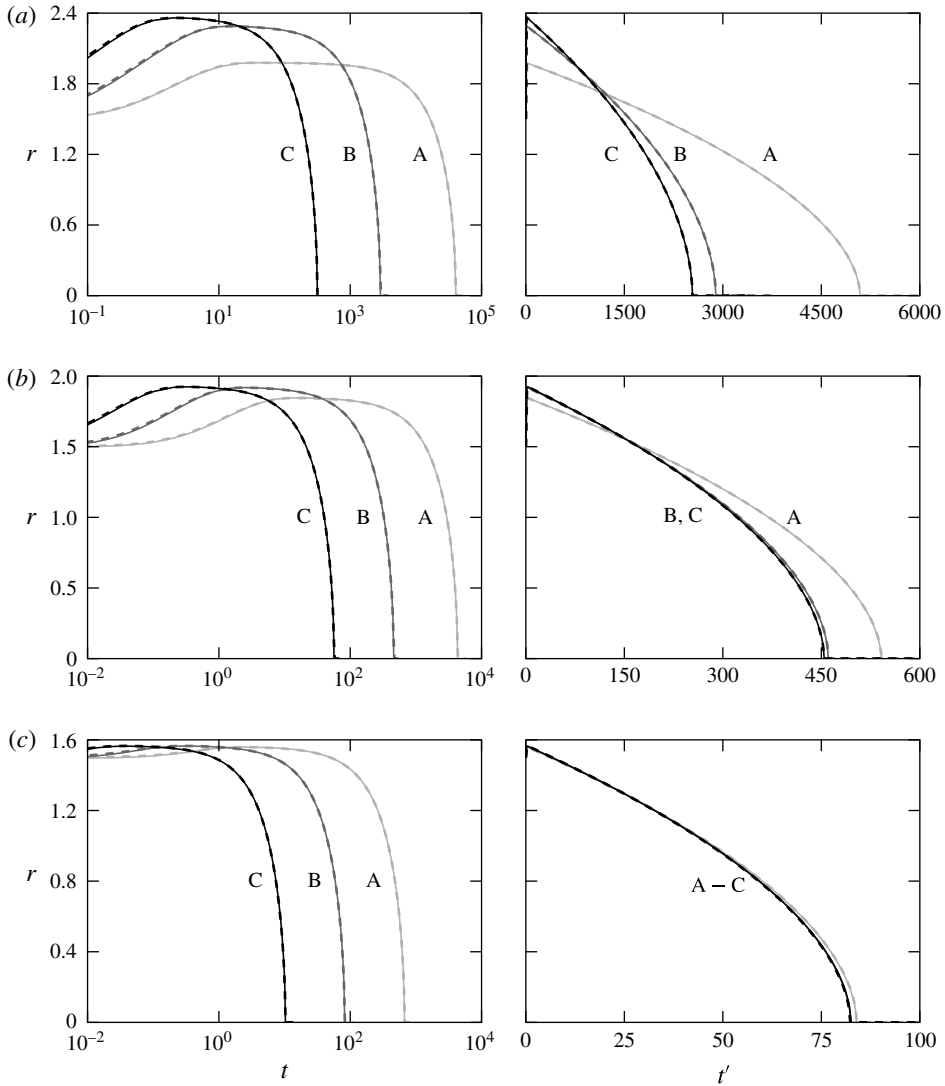
FIGURE 17. Influence of ϑ_s (set A: light grey curves $\vartheta_s = 20°$; set B: grey curves $\vartheta_s = 10°$; set C: black curves $\vartheta_s = 5°$). (*a*) $E = 0.125 \times 16^i$, $K = 14$, $\lambda = 2^{i+1} \times 10^{-5}$, $r(0) = 1.5$, $v(0) = 2^i$ where $i = 0, 1, 2$ for $\vartheta_s = 20°, 10°, 5°$, respectively, which corresponds to keeping the initial geometry and all physical parameters the same for all sets apart from ϑ_s. (*b*) As in (*a*) but with $E = 1.5 \times 16^i$. (*c*) As in (*a*) but with $E = 18 \times 16^i$. Left plots: r as a function of the dimensionless time, t; right plots: r as a function of the dimensionless time for set B, t'. In all plots solid and dashed curves correspond to the solutions to the full and reduced problems, respectively.

wetting regime. Indeed, this is a direct consequence of the fact that the inner region, where the influence of ϑ_s features more prominently, influences the dynamics through ϑ_m, whose value is dominated by the evaporation-induced contribution when $E \gg 1$. Hence as the apparent contact angle becomes close to ϑ_m during the comparatively longer evaporation stage, the influence of Young's angle, ϑ_s, becomes negligible.

4.7. *Apparent power laws*

The section concludes with some remarks on the apparent power-law behaviours characterising the evolution of the radius and volume of the droplet close to complete evaporation. In a typical experiment, it is observed that the time remaining until extinction is approximately proportional to the droplet radius raised to some power (see, e.g. Deegan *et al.* 2000; Shahidzadeh-Bonn *et al.* 2006; Cazabat & Guéna 2010, and the references therein). The theoretical prediction of these exponents, which sometimes deviate from the classical r^2-law (i.e. when the time remaining until extinction is proportional to the radius squared), was identified as one of the 'hot topics' discussed in the review of Bonn *et al.* (2009). As previously alluded to, the logarithmic dependencies which arose from our analysis also predict non-trivial (apparent) power laws. For example, if we consider $d(\ln t_*)/d(\ln v_0)$ using (4.4), we deduce that $t_* \sim v_0^n$, where n is given by

$$n = \frac{2}{3} - \frac{1}{3}\left(\ln\frac{\tilde{\beta}\theta_m^{2/3}v_0}{\lambda e^{1/2}}\right)^{-1} \approx \frac{2}{3} - \frac{1}{3}\left(\ln\frac{\tilde{\beta}\theta_m^{2/3}}{\lambda e^{1/2}}\right)^{-1}. \tag{4.8}$$

Clearly the 'local' exponent n depends on v_0 itself, but we may neglect v_0 appearing inside the logarithm by invoking a key assumption of our analysis, namely that the droplet is macroscopically large, or, equivalently, $r \gg r_c$. In all cases considered, this approximation works rather well. For example, the differences in the exponents obtained from fitting the data of figure 10(*a*) and the exponents computed from (4.8) were within $O(10^{-4})$.

From (4.8), we also see that for realistic values of the various parameters we always have $n < 2/3$ (recall that $n = 2/3$ corresponds to the classical r^2-law). Nevertheless, having exponents $n > 2/3$ is likely to become more feasible with the inclusion of additional effects which are neglected in the simple model of our study. Although a detailed parametric investigation of these apparent power laws is beyond the scope of this work, for the sake of completeness, we show a few representative calculations in figure 18 to reveal some qualitative trends about the dependence of the exponent a in $v \sim (t_* - t)^a$ on the system parameters using the calculation in figure 8 as a reference system. Looking at figure 18(*a*), we find that larger values of $\mathcal{K}$ increase a slightly, but they manifest themselves more strongly as the droplet shrinks, thus altering the power law as $t \to t_*$. Indeed, one would expect a power law of the form $v \sim (t_* - t)^3$ in the kinetically limited regime, where the global evaporation rate is proportional to the surface area of the droplet. This behaviour is observed here because using the larger value of $\mathcal{K}$ moves the onset of this regime to larger droplet sizes. From figure 18(*b*) we deduce that increasing $\mathcal{E}$ decreases a, but the change is generally negligibly small. Moreover, as we have seen in the preceding section, increasing λ speeds up the evaporation process and as a result we see an increase in the prefactor (figure 18*c*). In figures 18(*a–c*) we also plotted the apparent power law predicted by using $a = 1/n$ where n is given by the approximation (4.8). We readily see that the theoretical estimate predicts the overall trend quite well, provided that the volume of the droplet does not become too small. In figure 18(*d*) we explore the influence of gravity. Although its inclusion changes the exponent only at the onset (see the inset of figure 18*d*), this change can yield appreciable differences in t_* (for example, for the two simulations shown in figure 18*d*, the evaporative dynamics is approximately 1.5 times slower when $B = 0$ compared to $B = 10$).
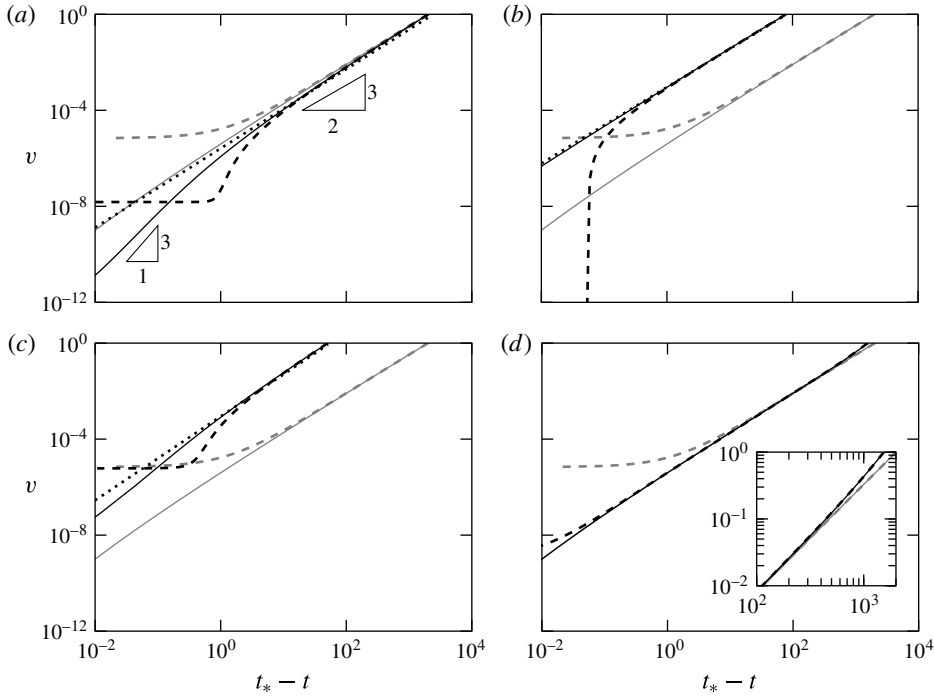
FIGURE 18. Plots of v as a function of $t_* - t$ for different sets of parameters. The solutions to the full problems and the corresponding reduced problems are shown by solid and dashed curves, respectively. In all plots, the grey curves correspond to the data obtained with $\mathcal{E} = 8 \times 10^{-5}$, $\mathcal{K} = 28 \times 10^{-5}$, $\lambda = 2 \times 10^{-5}$, $B = 0$ and $r(0) = v(0) = 1$, also plotted in figure 8. The black curves depict calculations where only one parameter is varied compared to the grey curves: (a) $\mathcal{K} = 28 \times 10^{-4}$ – the classical power laws are also shown for visual comparison; (b) $\mathcal{E} = 8 \times 10^{-3}$; (c) $\lambda = 2 \times 10^{-4}$; (d) $B = 10$. The dotted curves in (a–c) are based on power laws of the form $v \sim (t_* - t)^a$ where $a = 1/n$. The inset in (d) shows the volume evolution at early times.

A final observation that can be made by looking at the curves of figure 18 is the clear breakdown of our analytical theory (the dashed curves) when the volume of the droplet becomes small, but this only occurs when typically more than 99 % of the fluid of the droplet evaporates. This departure of the theory from the numerics is strongly dependent on the parameters of the problem (compare, e.g. the simulations shown in figure 18d), but ultimately, as expected from (3.40), the theory incorrectly predicts that the droplet stops evaporating when v reaches a (small) value in finite time.

5. Concluding remarks

In the present study, we have performed an asymptotic analysis of a minimal model describing the evaporative dynamics of thin partially wetting droplets in the Stokes flow regime. Our model contains the most basic ingredients needed to capture the essential physics of evaporation of droplets into a pure vapour atmosphere, requiring three parameters, slip, evaporation and kinetic resistance to evaporation, with gravity added as an extra parameter. A key new development in the present theory is the coupling of the micro- and macro-scales that allowed us to obtain a system

of differential equations for the radius and volume of the droplet for a one-sided evaporation model, which was previously studied asymptotically only in contrived settings (see, e.g. Anderson & Davis 1995; Hocking 1995).

By focusing on the limit when $\mathcal{E} = O(\lambda)$ as $\lambda \to 0$, the droplet dynamics was found to be governed by the universal contact line law at leading order (see (3.21)) and an appropriate evolution equation for the volume, utilising (3.38) with the baseline case $\mathcal{K} = O(\lambda)$. The latter equation can be replaced by (3.23), when $\lambda \ll \mathcal{K} \ll 1$ and $B = 0$. Particular emphasis was placed on treating the dynamics in the vicinity of the contact line and the evaporative term, which depends crucially on the droplet thickness. Thus, estimating the rate of mass loss required a detailed calculation which accounted for the contributions coming from the inner and outer regions.

A possibility for future work is to pursue other distinguished limits of the present model, e.g. when $\mathcal{K} = O(1)$ and $\mathcal{E} = O(1/|\ln \lambda|)$ as $\lambda \to 0$. This limit can possibly be physically relevant subject to the caveat that the modelling assumptions require the evaporative flux to be small with $\Delta\Theta \ll \Theta_0$. In such a case, departures from the universal contact line law may be observed, as elucidated by the asymptotic analysis of Oliver *et al.* (2015) for a model with constant mass flux, which applies to the distinguished limit of our model for droplets much smaller than the kinetic length, *s*.

In our analysis, we did not treat the contact line dynamics during the evaporation stage separately from the dynamics during the spreading stage, as in the recent work of Saxton *et al.* (2016). Instead, we assumed that the contact line law persists across both the spreading and the evaporation time scales. Although we gathered sufficient numerical evidence and offered some heuristic arguments why our approach may yield slightly better results as opposed to simply taking $\theta = \theta_m$ as done by Saxton *et al.* (2016), we have not undertaken a detailed error analysis to rigorously determine the accuracy of this step. For this to be done properly, it is likely that (3.21) must be generalised to include not only $\dot{r}$, but also $\dot{v}$ contributions giving rise to a reliable evaluation of the error made by taking $\theta = \theta_m$. Here, we found the contact line law to be consistently in excellent agreement with the predictions of the governing equations, thus avoiding the extra work described above.

The procedure we followed here can be readily adapted to other models that include additional effects (see, e.g. Ajaev 2005; Sodtke *et al.* 2008), which will most likely reduce to determining how they influence the parameters, β, $\tilde{\beta}$ and θ_m of the inner problem. This framework also applies if a precursor film model is used instead of a slip model. Unlike the non-volatile case, however, mapping the dynamics of different contact line models, be it a precursor film or a slip-based model, as done, for example, by Savva & Kalliadasis (2011) and Sibley *et al.* (2015*b*) is perhaps impossible due to the fact that from the inner region we need to extract the three aforementioned parameters; in contrast, in the non-volatile case only one parameter is extracted from the inner region, which allows us to easily map one model onto the other so that an asymptotic analysis followed by matching yields an identical set of differential equations at leading order.

We have demonstrated throughout this work the validity of our analysis, given that in all calculations we have performed the dynamics of the full problem was nearly indistinguishable from that of the reduced problem. Moreover, we managed to obtain a closed-form expression that enables the accurate prediction of the dynamics during

the evaporation stage and we were able to extract an expression for the evaporation time based on the system parameters, see (4.7). Our results also demonstrate that some of the non-trivial apparent power laws reported in experiments (see, e.g. Deegan *et al.* 2000) can be rationalised by the presence of the logarithm in (4.4), which can possibly modulate the exponent of a power law emerging from discrete data points.

The emphasis of the present work was placed on developing and verifying the asymptotic theory we have presented and no attempt was made to compare our results with the admittedly scarce experimental data reported in the literature. Moreover, in experiments the so-called constant radius mode is often observed (see, e.g. Cioulachtjian *et al.* 2010), whereby the contact angle decreases, but the contact line appears to be pinned. This pinning is apparently due to substrate heterogeneities, which are not accounted for in the present model. Our model, whose key assumption is that the substrate is free from heterogeneities, is only able to capture the constant contact angle mode, during which the contact line is freely receding in the evaporation stage, whereas the contact angle remains constant above its equilibrium value determined by Young's relation. To date, this remains an important question in the field, namely how the selection occurs between a pinned contact line ('constant contact radius' mode) and freely receding contact line ('constant contact angle' mode) (Bourges-Monnier & Shanahan 1995; Semenov *et al.* 2014; Stauber *et al.* 2014, 2015). It is clear, however, that explicitly accounting for the substrate heterogeneities will be instrumental for capturing the transition between the two modes and providing an accurate description of the underlying contact line dynamics. This and related topics will be subjects of future investigations.

Acknowledgements

Appendix A. Weakly modified Young's angles

When $E \ll 1$ and $K = O(1)$, θ_m is weakly modified by evaporation, so that have $\theta_m \approx 1$ at leading order. Given also that in the present study we have $\dot{r} \ll 1$, we introduce an inner expansion of the form

$$\phi \sim \eta + \tilde{\phi} + \cdots, \tag{A 1}$$

where $\tilde{\phi}$ retains the linear terms in E and $\dot{r}$ so that we can take $\eta \gg \tilde{\phi}$. The linearised differential equation for $\tilde{\phi}$ satisfies

$$\dot{r} + \partial_\eta [\eta^2 (\eta + 1) \partial_\eta^3 \tilde{\phi}] = -\frac{E}{\eta + K}, \tag{A 2}$$

which is to be solved subject to the homogeneous conditions at $\eta = 0$, namely

$$\tilde{\phi} = \partial_\eta \tilde{\phi} = 0 \tag{A 3}$$

and possesses the following asymptotic behaviour as $\eta \to \infty$:

$$\partial_\eta \tilde{\phi} \sim \alpha E + \dot{r} \ln(\beta \eta), \tag{A 4}$$

where α and β are constants to be determined. Hence, it follows that in the weak evaporation limit, the modified Young's angle is approximately given by

$$\theta_m = 1 + \alpha E. \tag{A 5}$$

Integrating (A 2) once and requiring that both sides vanish as $\eta \to 0$, gives, after some term rearrangement

$$\frac{\dot{r}}{\eta + 1} + \eta \partial_\eta^3 \tilde{\phi} = -\frac{E}{\eta(\eta + 1)} \ln \frac{\eta + K}{K}. \tag{A 6}$$

Integration by parts for η ranging from 0 to some large scale $\ell \gg 1$ gives

$$[\eta \partial_\eta^2 \tilde{\phi} - \partial_\eta \tilde{\phi}]_0^\ell + \dot{r} \ln(\ell + 1) = -E \int_0^\ell \frac{1}{\eta(\eta + 1)} \ln \frac{\eta + K}{K} \, \mathrm{d}\eta. \tag{A 7}$$

From (A 3) we must have $\eta \partial_\eta^2 \tilde{\phi} \to 0$ as $\eta \to 0$, whereas (A 4) gives $\eta \partial_\eta^2 \tilde{\phi} \sim \dot{r}$ as $\eta \to \infty$. Hence, by standard manipulations, it is easy to see from (A 7) that the constants α and β in (A 4) are

$$\alpha = \int_0^\infty \frac{1}{\eta(\eta + 1)} \ln \frac{\eta + K}{K} \, \mathrm{d}\eta = \mathrm{dilog}\, K + \frac{1}{2} \ln^2 K + \frac{\pi^2}{6}, \tag{A 8}$$

$$\beta = \mathrm{e}, \tag{A 9}$$

where $\mathrm{dilog}\, K$ denotes the dilogarithm function, which is defined as

$$\mathrm{dilog}\, K = \int_1^K \frac{\ln x}{1 - x} \, \mathrm{d}x. \tag{A 10}$$

From the asymptotics of the inner region, we need to have $\alpha E \ll 1$, which restricts the regime of validity of the calculation presented here. Using the small- and large-K expansions of α we find that if K is small, good agreement is expected if E is chosen so that

$$E \ll \frac{6}{2\pi^2 + 3 \ln^2 K}, \tag{A 11}$$

whereas if K is large, it suffices to choose

$$E \ll \frac{K}{1 + \ln K}. \tag{A 12}$$

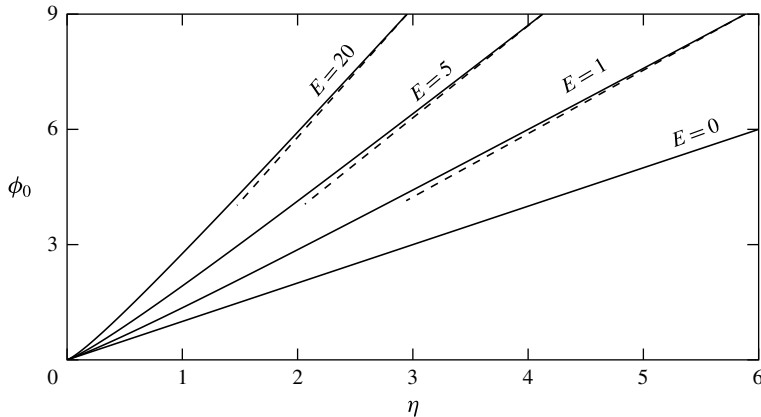This shows that (A 5) can be an acceptable approximation to θ_m provided that K is sufficiently large, even when $E = O(1)$.

FIGURE 19. Plots of ϕ_0 as a function of η for $K = 1$ and different values of E. The dashed lines show the asymptotic slope, θ_m.

Appendix B. Numerical solution of boundary value problems arising in the analysis

B.1. *Boundary value problem for θ_m*

In order to determine θ_m, we solve (3.15) with (3.16) numerically. Noting that (3.15) does not depend explicitly on the independent variable, η, a change of the independent variable to ϕ_0 leads to the lower-order differential equation

$$F\partial_{\phi_0}[\phi_0^2(\phi_0 + 1)F\partial_{\phi_0}(F\partial_{\phi_0}F)] = -\frac{E}{\phi_0 + K}, \tag{B 1}$$

where we set $F = \partial_\eta \phi_0$. This is a differential equation for $F(\phi_0)$ to be solved along with $\partial_{\phi_0} F \to 0$ and $\partial_{\phi_0}^2 F \to 0$ as $\phi_0 \to \infty$, as well as $F(0) = 1$. A straightforward calculation reveals that the order of (B 1) is equal to the sum of the degrees of freedom in the local expansions of F as $\phi_0 \to 0$ and as $\phi_0 \to \infty$, one of which is θ_m.

The advantage of this variable change is that it facilitates the extraction of θ_m, by simply obtaining the value of F as $\phi_0 \to \infty$ (or, equivalently, $\eta \to \infty$) as part of the numerical solution, instead of finding θ_m from a non-constant asymptotic behaviour. This calculation was completed numerically using the pseudo-spectral collocation method (Boyd 2000; Trefethen 2000), noting that in order to avoid the logarithmic singularity of $\partial_{\phi_0} F$ at $\phi_0 = 0$, we introduced yet another change of variable $y = \ln \phi_0$ with $y \in (-\infty, \infty)$, which was then mapped appropriately to the interval $[-1, 1]$ of the Chebyshev collocation points. By doing so, the derivatives with respect to y are well defined everywhere and, at the same time, we also manage to avoid domain truncation and the use of a shooting method to achieve the desired behaviour at infinity. In this manner, we form a nonlinear boundary value problem on the interval $[-1, 1]$ which is solved with Newton iterations. One can then obtain $\phi_0(\eta)$ from the implicit formula $\eta = \int_0^{\phi_0} d\varphi / F(\varphi)$. The results of such calculations are shown in figure 19, where we plot ϕ_0 as a function of η. The plots confirm that in all cases the free surface meets the substrate with a unit slope, i.e. the curves approach the origin tangentially to the $E = 0$ line, $\phi_0 = \eta$. At short distances away from the contact line, the free surface bends abruptly, with its slope approaching θ_m as $\eta \to \infty$.
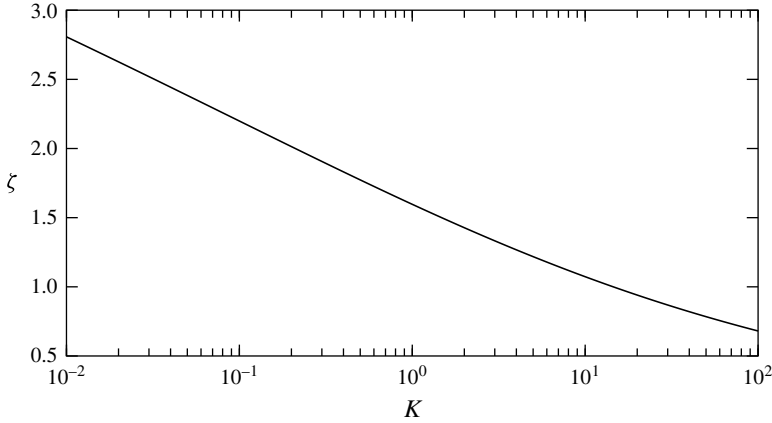
FIGURE 20. Plot of ζ as a function of K describing the large-E asymptotics of $\theta_m \sim \zeta(K)E^{1/4}$.

B.2. *Boundary value problem for $\zeta(K)$*

To obtain $\zeta(K)$ numerically, we eliminate E from (B 1) by considering the equation for $\tilde{F}(\phi_0) = E^{-1/4}F(\phi_0)$. This merely changes the aforementioned conditions on F to $\tilde{F}(0) = E^{-1/4}$ at $\phi_0 = 0$, whereas the condition at infinity, $\partial_{\phi_0}\tilde{F} \to 0$, stays the same. In this manner, if we formally take the limit $E \to \infty$, $\tilde{F}(0) \to 0$ and we can obtain $\zeta(K)$ from the value of $\tilde{F}$ as $\phi_0 \to \infty$ which is well defined for non-zero K (see figure 20). Such a formulation corresponds to a perfectly wetting scenario, i.e. with zero ϑ_s. Although the perfectly wetting case is interesting in its own right (e.g. we can easily verify that ϕ_0 scales with $\eta^{4/3}$ as $\eta \to 0$), it is not pursued further in the present study.

B.3. *Boundary value problem for β*

Proceeding analogously to the method utilised to obtain θ_m (see appendix B.1), we take ϕ_0 as the dependent variable so that (3.18) becomes:

$$\mathcal{L}[\phi_1] + 1 = 0, \tag{B 2}$$

where we defined the differential operator

$$\begin{aligned}
\mathcal{L}[\cdot] = {} & \partial_{\phi_0}\{\phi_0^2(\phi_0 + 1)F\partial_{\phi_0}[F\partial_{\phi_0}(F\partial_{\phi_0}[\cdot])] + \phi_0(3\phi_0 + 2)F\partial_{\phi_0}(F\partial_{\phi_0}F)[\cdot]\} \\
& - \frac{E[\cdot]}{F(\phi_0 + K)^2}.
\end{aligned} \tag{B 3}$$

Even though (B 2) is a more complicated differential equation compared to (3.18), we note that it is a linear one, with its coefficients depending on the solution to (B 1). Changing the dependent variable from η to ϕ_0 transforms the condition (3.19b) to

$$\partial_{\phi_0}\phi_1 \sim \frac{1}{\theta_m^3}\ln\frac{\beta\phi_0}{\theta_m}, \tag{B 4}$$

which is equivalent to having

$$\phi_1 \sim \frac{\phi_0}{\theta_m^3}\ln\frac{\beta\phi_0}{\theta_m\mathrm{e}} \tag{B 5}$$

as $\phi_0 \to \infty$. As before, we use the mapping $\phi_0 = e^y$ to solve for β. We also exploit the linearity of (B 2), casting it as a problem for $\psi(y)$, where $\psi(y)$ is defined from

$$\phi_1 = e^y \left(\psi(y) + \frac{y}{\theta_m^3} \frac{e^y}{e^y + 1} \right), \tag{B 6}$$

and is subject to homogeneous conditions as $y \to \pm\infty$, namely $\psi = \partial_y \psi = 0$ as $y \to -\infty$ and $\partial_y \psi = \partial_y^2 \psi = 0$ as $y \to \infty$. By doing so, we avoid dealing with ϕ_1 becoming unbounded as $\phi_0 \to \infty$, while at the same time, we can extract β, since from (B 5) and (B 6) we have $\psi \to \psi_\infty$ as $y \to \infty$, so that

$$\psi_\infty = \frac{1}{\theta_m^3} \ln \frac{\beta}{\theta_m e}. \tag{B 7}$$

The value of β is readily found from (B 7), i.e.

$$\beta = \theta_m e^{1 + \psi_\infty \theta_m^3}. \tag{B 8}$$

Appendix C. Numerical solution of the full and reduced problems

Solving (3.21) and (3.38) with (3.5) subject to initial conditions $r(0) = r_0$ and $v(0) = v_0$ (typically we consider cases with $v_0 = 1$) is rather straightforward, once we have the values of $\tilde{\beta}$, β and θ_m from the asymptotics of the inner region (see discussion in §§ 3.1.2 and 3.2). For time stepping, a standard Runge–Kutta scheme suffices for accurate solutions, evaluating the integrals of δ and γ, equations (3.10) and (3.39), respectively, using the Legendre–Gauss quadrature (see Abramowitz & Stegun 1972, § 25.4).

On the other hand, the original partial differential equation, equation (2.14), is a free-boundary problem and is considerably more difficult to solve, due to the boundary layers present at $x = r(t)$ which make the problem rather stiff particularly for smaller values of λ. Moreover, enforcing the condition (2.18*e*) is impossible by standard numerical methods as it requires $\partial_x^3 h$ to be singular for $h \partial_x^3 h$ to be finite as $x \to r(t)$. To remedy these difficulties, we use similar ideas as in Savva & Kalliadasis (2009), thus transforming the governing equation into a fixed boundary problem by an appropriate mapping and casting it in the form of an integral partial differential equation, which is solved in MATLAB.

More specifically, we introduce the mapping $x = yr(t)$, where $0 \leqslant y \leqslant 1$, multiply (2.14) by y and integrate the resulting equation from 0 to y so that we obtain

$$\partial_t g + \frac{\dot{r}}{r}(2g - y\partial_y g) + \frac{1}{r^4} yh^2(h + \lambda)\partial_y \left(\partial_y^2 h + \frac{1}{y}\partial_y h - Br^2 h \right) + j = 0, \tag{C 1}$$

where

$$g(y, t) = \int_0^y \tilde{y}h(\tilde{y}, t)\,\mathrm{d}\tilde{y} \quad \text{and} \quad j(y, t) = \int_0^y \frac{E\lambda\tilde{y}}{h(\tilde{y}, t) + K\lambda}\,\mathrm{d}\tilde{y}. \tag{C 2a,b}$$

In (C 1) and (C 2*b*), $h(y, t)$ is evaluated from

$$h = y^{-1}\partial_y g. \tag{C 3}$$

Hence, in this new formulation, we solve for $g(y, t)$ instead of $h(y, t)$, which is determined by the formula above. The axisymmetric geometry requires $g(y, t)$ to be an even function of y i.e. we require that at $y = 0$ we have

$$\partial_y g = 0 \quad \text{and} \quad \partial_y^3 g = 0, \qquad (C\,4a,b)$$

together with the boundary conditions of the original problem at $x = r$, equations (2.18a) and (2.18b), being transformed to conditions at $y = 1$,

$$\partial_y g = 0 \quad \text{and} \quad \partial_y^2 g = -r, \qquad (C\,4c,d)$$

respectively. However, the condition prescribing the velocity of the contact line of the original problem, equation (2.18e), which was essentially a derived explicit equation for the velocity of the free boundary at the contact line, is no longer practicable. This is because (C 1) is a fourth-order problem in y for g and (2.18e) requires the evaluation of $\partial_y^4 g$ at $y = 1$. However, the usefulness of (2.18e) in the present context is that it explicitly shows that $h\partial_y^3 h$ remains finite and hence the third term on the left-hand side of (C 1) vanishes at the contact line, as $y \to 1$. Therefore, to complete the set of conditions for the reformulated problem, equation (C 1) turns out to be compatible (asymptotically as $y \to 1$) with the following condition

$$g = \frac{v}{r^2} \qquad (C\,4e)$$

at $y = 1$, which follows from (C 2a) evaluated at $y = 1$, equation (2.19) and the definition $y = x/r$; lastly

$$\dot{v} = -r^2 j(1, t), \qquad (C\,5)$$

which is essentially (2.20) rewritten with the help of (C 2b). The new problem, equations (C 1) and (C 5) subject to the boundary conditions (C 4) is less stiff to solve compared to the original problem given that only the third spatial derivative of h needs to be computed, instead of the fourth derivative in (2.14).

The governing equation is discretised in space using the Chebyshev pseudo-spectral collocation method, which naturally clusters more points near the contact line. It is also important to note that the discretisation is done over the interval $-1 \leqslant y \leqslant 1$ using an even number of collocation points to avoid complications at the axis of symmetry, $y = 0$. In the end, the solution is computed for $0 \leqslant y \leqslant 1$ only, having discarded the remaining points due to symmetry (see, e.g. Trefethen 2000). By doing so, we achieve symmetry about $y = 0$ in the computed solution, without imposing explicitly the symmetry condition of the original problem, equation (2.18c,d). The spatially discretised problem is solved using the method of lines. Noteworthy is also that since we no longer use an explicit equation for $\dot{r}$, but an additional condition on g, equation (C 4e), the problem is most appropriately cast as a system of differential algebraic equations.

As an initial droplet shape we use

$$h(y, 0) = \left[m + \left(\frac{1}{\theta} - m \right) \frac{1}{1 + (1 - y^2)\epsilon^{-1}} \right] h_0(yr_0), \qquad (C\,6)$$

for some numerical parameter $\epsilon \ll 1$ and specified values for $r_0 = r(0)$ and $v_0 = v(0)$, where h_0 and θ are given by substituting $r = r_0$ and $v = v_0$ in (3.4) and (3.5), respectively, and $m \approx 1$ is found by computing

$$m = \frac{v_0 - \theta^{-1}S}{v_0 - S} \quad \text{with} \quad S = r_0^2 \int_0^1 \frac{yh_0(yr_0)}{1 + (1 - y^2)\epsilon^{-1}} \, dy \qquad (C\,7)$$

to ensure that the initial volume condition $v(0) = v_0$ is satisfied. However, just setting $m = 1$ is usually sufficient when $\epsilon = O(\lambda)$ since the deviations from v_0 are very small, typically within 0.1 % of the actual value of v_0. The initial condition given by (C 6) satisfies the requirement that the free surface must meet the substrate at Young's angle, whilst the bulk is well approximated by the leading-order outer solution. By choosing such an initial shape with $\epsilon = O(\lambda)$, we avoid the transient dynamics necessary for an arbitrarily shaped free surface to relax approximately to the quasi-static shape in the bulk (see also the last paragraph of § 3.1). Unless otherwise specified, in our simulations we chose $\epsilon = 0.1 \gg \lambda$ to demonstrate that these transients are rather brief. Besides, even if the initial free surface shape is significantly different from the leading-order, quasi-static solution, equation (3.4), we found that the droplet reaches the quasi-static regime within $t = O(10^{-1})$.

Lastly, we should mention that solving numerically the governing partial differential equation becomes increasingly stiffer as the droplet evaporates, because the mesh points get crammed in a smaller and smaller spatial domain. For this reason, we usually do a three-step computation, stopping the calculation twice, when r becomes 10^{-1} and 10^{-2}, mapping some of the mesh points away from the contact line region towards the bulk of the droplet and restarting the computation with an initial condition obtained by utilising the polynomial interpolant associated with the collocation scheme of the previous step. Ultimately, we terminate the computation when the droplet radius becomes $O(10^{-4})$ since further mesh adaptivity does not help much with regards to the stiffness of the problem. Besides, at this stage $v(t) = O(10^{-12})$, whose evolution is beyond the scope of the macroscopic analysis we presented. Thus, we did not deem continuing the computation necessary for smaller values of the radius. The time at which the droplet will completely evaporate, denoted by t_*, is a singular limit for the partial differential equation. Even though the evaporation time is expected to be very close to the time at which a computation is terminated, it was estimated by extrapolating the droplet radius to zero by simply using the last data points recorded for the radius, say (t_1, r_1) and (t_2, r_2). Then t_* is estimated by fitting a square root through the points so that the slope of $r(t)$ becomes infinite at t_*. We find

$$t_* \approx \frac{r_1^2 t_2 - r_2^2 t_1}{r_1^2 - r_2^2}. \tag{C 8}$$

In all cases we tested, this simple formula gave results that were within 0.01 % of the value returned by including more data points and using a more involved extrapolation method, such as Neville's extrapolation algorithm (Press *et al.* 1992). It should be emphasised, however, that (C 8) is merely used as a numerical tool to get a closer estimate to t_* and we do not actually claim a square-root law at the singular limit of the problem.

REFERENCES

ABRAMOWITZ, M. & STEGUN, I. A. 1972 *Handbook of Mathematical Functions with Formulas, Graphs, and Mathematical Tables*. Dover.

AJAEV, V. S. 2005 Spreading of thin volatile liquid droplets on uniformly heated surfaces. *J. Fluid Mech.* **528**, 279–296.

ANDERSON, D. M. & DAVIS, S. H. 1995 The spreading of volatile liquid droplets on heated surfaces. *Phys. Fluids* **7** (2), 248–265.

BONN, D., EGGERS, J., INDEKEU, J., MEUNIER, J. & ROLLEY, E. 2009 Wetting and spreading. *Rev. Mod. Phys.* **81** (2), 739–805.

BOURGES-MONNIER, C. & SHANAHAN, M. E. R. 1995 Influence of evaporation on contact angle. *Langmuir* **11** (7), 2820–2829.

BOYD, J. P. 2000 *Chebyshev and Fourier Spectral Methods*, 2nd edn. Dover.

BRUTIN, D. (Ed.) 2015 *Droplet Wetting and Evaporation: From Pure to Complex Fluids*, 1st edn. Academic.

BURELBACH, J. P., BANKOFF, S. G. & DAVIS, S. H. 1988 Nonlinear stability of evaporating/condensing liquid films. *J. Fluid Mech.* **195**, 463–494.

CAREY, V. P. 2007 *Liquid–Vapor Phase-Change Phenomena: An Introduction to the Thermophysics of Vaporization and Condensation Processes in Heat Transfer Equipment*, 2nd edn. CRC Press.

CAZABAT, A.-M. & GUÉNA, G. 2010 Evaporation of macroscopic sessile droplets. *Soft Matt.* **6** (12), 2591–2612.

CHOI, K., NG, A. H. C., FOBEL, R. & WHEELER, A. R. 2012 Digital microfluidics. *Annu. Rev. Anal. Chem.* **5** (1), 413–440.

CIOULACHTJIAN, S., LAUNAY, S., BODDAERT, S. & LALLEMAND, M. 2010 Experimental investigation of water drop evaporation under moist air or saturated vapour conditions. *Intl J. Therm. Sci.* **49** (6), 859–866.

COLINET, P. & REDNIKOV, A. 2011 On integrable singularities and apparent contact angles within a classical paradigm. *Eur. Phys. J. Spec. Topics* **197** (1), 89–113.

COX, R. G. 1986 The dynamics of the spreading of liquids on a solid surface. Part 1. Viscous flow. *J. Fluid Mech.* **168**, 169–194.

DAVIDOVITS, P., WORSNOP, D. R., JAYNE, J. T., KOLB, C. E., WINKLER, P., VRTALA, A., WAGNER, P. E., KULMALA, M., LEHTINEN, K. E. J., VESALA, T. & MOZURKEWICH, M. 2004 Mass accommodation coefficient of water vapor on liquid water. *Geophys. Res. Lett.* **31** (22), L22111.

DAVIS, S. H. & HOCKING, L. M. 1999 Spreading and imbibition of viscous liquid on a porous base. *Phys. Fluids* **11** (1), 48–57.

DEEGAN, R. D., BAKAJIN, O., DUPONT, T. F., HUBER, G., NAGEL, S. R. & WITTEN, T. A. 1997 Capillary flow as the cause of ring stains from dried liquid drops. *Nature* **389** (6653), 827–829.

DEEGAN, R. D., BAKAJIN, O., DUPONT, T. F., HUBER, G., NAGEL, S. R. & WITTEN, T. A. 2000 Contact line deposits in an evaporating drop. *Phys. Rev. E* **62** (1), 756–765.

DEHAECK, S., REDNIKOV, A. & COLINET, P. 2014 Vapor-based interferometric measurement of local evaporation rate and interfacial temperature of evaporating droplets. *Langmuir* **30** (8), 2002–2008.

DUGAS, V., BROUTIN, J. & SOUTEYRAND, E. 2005 Droplet evaporation study applied to DNA chip manufacturing. *Langmuir* **21** (20), 9130–9136.

DUNN, G. J., WILSON, S. K., DUFFY, B. R., DAVID, S. & SEFIANE, K. 2009 The strong influence of substrate conductivity on droplet evaporation. *J. Fluid Mech.* **623**, 329–351.

EAMES, I. W., MARR, N. J. & SABIR, H. 1997 The evaporation coefficient of water: a review. *Intl J. Heat Mass Transfer* **40** (12), 2963–2973.

EGGERS, J. 2005*a* Contact line motion for partially wetting fluids. *Phys. Rev. E* **72** (6), 061605.

EGGERS, J. 2005*b* Existence of receding and advancing contact lines. *Phys. Fluids* **17** (8), 082106.

EGGERS, J. & PISMEN, L. M. 2010 Nonlocal description of evaporating drops. *Phys. Fluids* **22** (11), 112101.

ERBIL, H. Y. 2012 Evaporation of pure liquid sessile and spherical suspended drops: a review. *Adv. Colloid Interface Sci.* **170** (1–2), 67–86.

GELDERBLOM, H., BLOEMEN, O. & SNOEIJER, J. H. 2012 Stokes flow near the contact line of an evaporating drop. *J. Fluid Mech.* **709**, 69–84.

DE GENNES, P.-G. 1985 Wetting: statics and dynamics. *Rev. Mod. Phys.* **57** (3), 827–863.

GIRARD, F., ANTONI, M. & SEFIANE, K. 2008 On the effect of Marangoni flow on evaporation rates of heated water drops. *Langmuir* **24** (17), 9207–9210.

GOKHALE, S. J., PLAWSKY, J. L. & WAYNER, P. C. 2003 Experimental investigation of contact angle, curvature, and contact line motion in dropwise condensation and evaporation. *J. Colloid Interface Sci.* **259** (2), 354–366.

HERVET, H. & DE GENNES, P.-G. 1984 The dynamics of wetting: precursor films in the wetting of 'dry' solids. *C. R. Acad. Sci. Paris* **299**, 499–503.

HOCKING, L. M. 1983 The spreading of a thin drop by gravity and capillarity. *Q. J. Mech. Appl. Maths* **36** (1), 55–69.

HOCKING, L. M. 1992 Rival contact-angle models and the spreading of drops. *J. Fluid Mech.* **239**, 671–781.

HOCKING, L. M. 1995 On contact angles in evaporating liquids. *Phys. Fluids* **7** (12), 2950–2955.

HU, H. & LARSON, R. G. 2006 Marangoni effect reverses coffee-ring depositions. *J. Phys. Chem.* B **110** (14), 7090–7094.

HUH, C. & SCRIVEN, L. E. 1971 Hydrodynamic model of steady movement of a solid/liquid/fluid contact line. *J. Colloid Interface Sci.* **35** (1), 85–101.

JANEČEK, V. & NIKOLAYEV, V. S. 2012 Contact line singularity at partial wetting during evaporation driven by substrate heating. *Europhys. Lett.* **100** (1), 14003.

KELLY-ZION, P. L., PURSELL, C. J., BOOTH, R. S. & VANTILBURG, A. N. 2009 Evaporation rates of pure hydrocarbon liquids under the influences of natural convection and diffusion. *Intl J. Heat Mass Transfer* **52** (13–14), 3305–3313.

KIM, J. 2007 Spray cooling heat transfer: the state of the art. *Intl J. Heat Fluid Flow* **28** (4), 753–767.

KING, J. R. 2001 Thin-film flows and high-order degenerate parabolic equations. In *IUTAM Symposium on Free Surface Flows* (ed. A. C. King & Y. D. Shikhmurzaev), pp. 7–18. Springer.

LACEY, A. A. 1982 The motion with slip of a thin viscous droplet over a solid surface. *Stud. Appl. Maths* **67** (3), 217–230.

LAUGA, E., BRENNER, M. & STONE, H. 2007 Microfluidics: the no-slip boundary condition. In *Springer Handbook of Experimental Fluid Mechanics* (ed. C. Tropea, A. L. Yarin & J. F. Foss), chap. 19, pp. 1219–1240. Springer.

LOPES, M. C., BONACCURSO, E., GAMBARYAN-ROISMAN, T. & STEPHAN, P. 2013 Influence of the substrate thermal properties on sessile droplet evaporation: effect of transient heat transport. *Colloids Surf.* A **432**, 64–70.

MAREK, R. & STRAUB, J. 2001 Analysis of the evaporation coefficient and the condensation coefficient of water. *Intl J. Heat Mass Transfer* **44** (1), 39–53.

MOOSMAN, S. & HOMSY, G. M. 1980 Evaporating menisci of wetting fluids. *J. Colloid Interface Sci.* **73** (1), 212–223.

MORRIS, S. J. S. 2001 Contact angles for evaporating liquids predicted and compared with existing experiments. *J. Fluid Mech.* **432**, 1–30.

MURISIC, N. & KONDIC, L. 2011 On evaporation of sessile drops with moving contact lines. *J. Fluid Mech.* **679**, 219–246.

OLIVER, J. M., WHITELEY, J. P., SAXTON, M. A., VELLA, D., ZUBKOV, V. S. & KING, J. R. 2015 On contact-line dynamics with mass transfer. *Eur. J. Appl. Maths* **26**, 1–49.

PAUL, B. 1962 Compilation of evaporation coefficients. *ARS J.* **32** (9), 1321–1328.

PISMEN, L. & EGGERS, J. 2008 Solvability condition for the moving contact line. *Phys. Rev.* E **78** (5), 056304.

PLAWSKY, J. L., PANCHAMGAM, S. S., GOKHALE, S. J., WAYNER, P. C. & DASGUPTA, S. 2004 A study of the oscillating corner meniscus in a vertical constrained vapor bubble system. *Superlattices Microstruct.* **35** (3–6), 559–572.

POTASH, M. & WAYNER, P. C. 1972 Evaporation from a two-dimensional extended meniscus. *Intl J. Heat Mass Transfer* **15** (10), 1851–1863.

POULARD, C., GUÉNA, G. & CAZABAT, A. M. 2005 Diffusion-driven evaporation of sessile drops. *J. Phys.: Condens. Matter* **17** (49), S4213–S4227.

PRESS, W., TEUKOLSKY, S., VETTERLING, W. & FLANNERY, B. 1992 *Numerical Recipes in C*, 2nd edn. chap. 3.1, pp. 108–110. Cambridge University Press.

RAJ, R., KUNKELMANN, C., STEPHAN, P., PLAWSKY, J. & KIM, J. 2012 Contact line behavior for a highly wetting fluid under superheated conditions. *Intl J. Heat Mass Transfer* **55** (9–10), 2664–2675.

REDNIKOV, A. & COLINET, P. 2013 Singularity-free description of moving contact lines for volatile liquids. *Phys. Rev.* E **87** (1), 010401.

REDNIKOV, A. Y. & COLINET, P. 2011 Truncated versus extended microfilm at a vapor–liquid contact line on heated substrate. *Langmuir* **27** (5), 1758–1769.

REDNIKOV, A. Y., ROSSOMME, S. & COLINET, P. 2009 Steady microstructure of a contact line for a liquid on a heated surface overlaid with its pure vapor: parametric study for a classical model. *Multiphase Sci. Technol.* **21** (3), 213–248.

REN, W., TRINH, P. H. & WEINAN, E. 2015 On the distinguished limits of the Navier slip model of the moving contact line problem. *J. Fluid Mech.* **772**, 107–126.

RISTENPART, W. D., KIM, P. G., DOMINGUES, C., WAN, J. & STONE, H. A. 2007 Influence of substrate conductivity on circulation reversal in evaporating drops. *Phys. Rev. Lett.* **99** (23), 234502.

SAVVA, N. & KALLIADASIS, S. 2009 Two-dimensional droplet spreading over topographical substrates. *Phys. Fluids* **21** (9), 092102.

SAVVA, N. & KALLIADASIS, S. 2011 Dynamics of moving contact lines: a comparison between slip and precursor film models. *Europhys. Lett.* **94** (6), 64004.

SAVVA, N. & KALLIADASIS, S. 2012 Influence of gravity on the spreading of two-dimensional droplets over topographical substrates. *J. Engng Maths* **73** (1), 3–16.

SAVVA, N. & KALLIADASIS, S. 2013 Droplet motion on inclined heterogeneous substrates. *J. Fluid Mech.* **725**, 462–491.

SAVVA, N. & KALLIADASIS, S. 2014 Low-frequency vibrations of two-dimensional droplets on heterogeneous substrates. *J. Fluid Mech.* **754**, 515–549.

SAVVA, N., REDNIKOV, A. & COLINET, P. 2014 Asymptotic analysis of evaporating droplets. In *Proceedings of the 4th Micro and Nano Flows Conference, University College, London, UK* (ed. T. Karayiannis, C. S. König & S. Balabani), p. 236. Brunel University.

SAXTON, M. A., WHITELEY, J. P., VELLA, D. & OLIVER, J. M. 2016 On thin evaporating drops: when is the d^2-law valid? *J. Fluid Mech.* **792**, 134–167.

SCHRAGE, R. 1953 *A Theoretical Study of Interphase Mass Transfer*. Columbia University Press.

SCHWARTZ, L. W. & ELEY, R. R. 1998 Simulation of droplet motion on low-energy and heterogeneous surfaces. *J. Colloid Interface Sci.* **202** (1), 173–188.

SEFIANE, K., MOFFAT, J. R., MATAR, O. K. & CRASTER, R. V. 2008 Self-excited hydrothermal waves in evaporating sessile drops. *Appl. Phys. Lett.* **93** (7), 074103.

SEMENOV, S., TRYBALA, A., RUBIO, R. G., KOVALCHUK, N., STAROV, V. & VELARDE, M. G. 2014 Simultaneous spreading and evaporation: recent developments. *Adv. Colloid Interface Sci.* **206**, 382–398.

SHAHIDZADEH-BONN, N., RAFAÏ, S., AZOUNI, A. & BONN, D. 2006 Evaporating droplets. *J. Fluid Mech.* **549**, 307–313.

SHIKHMURZAEV, Y. D. 2008 *Capillary Flows with Forming Interfaces*. Taylor & Francis.

SIBLEY, D. N., NOLD, A. & KALLIADASIS, S. 2015*a* The asymptotics of the moving contact line: cracking an old nut. *J. Fluid Mech.* **764**, 445–462.

SIBLEY, D. N., NOLD, A., SAVVA, N. & KALLIADASIS, S. 2013 On the moving contact line singularity: asymptotics of a diffuse-interface model. *Eur. Phys. J.* E **36** (3), 26.

SIBLEY, D. N., NOLD, A., SAVVA, N. & KALLIADASIS, S. 2015*b* A comparison of slip, disjoining pressure, and interface formation models for contact line motion through asymptotic analysis of thin two-dimensional droplet spreading. *J. Engng Maths* **94**, 19–41.

SIBLEY, D. N., SAVVA, N. & KALLIADASIS, S. 2012 Slip or not slip? A methodical examination of the interface formation model using two-dimensional droplet spreading on a horizontal planar substrate as a prototype system. *Phys. Fluids* **24** (8), 082105.

SOBAC, B. & BRUTIN, D. 2012 Thermocapillary instabilities in an evaporating drop deposited onto a heated substrate. *Phys. Fluids* **24** (3), 032103.

SODTKE, C., AJAEV, V. S. & STEPHAN, P. 2008 Dynamics of volatile liquid droplets on heated surfaces: theory versus experiment. *J. Fluid Mech.* **610**, 343–362.

STAUBER, J. M., WILSON, S. K., DUFFY, B. R. & SEFIANE, K. 2014 On the lifetimes of evaporating droplets. *J. Fluid Mech.* **744**, R2.

STAUBER, J. M., WILSON, S. K., DUFFY, B. R. & SEFIANE, K. 2015 On the lifetimes of evaporating droplets with related initial and receding contact angles. *Phys. Fluids* **27** (12), 122101.

STEPHAN, P. C. & BUSSE, C. A. 1992 Analysis of the heat transfer coefficient of grooved heat pipe evaporator walls. *Intl J. Heat Mass Transfer* **35** (2), 383–391.

TODOROVA, D., THIELE, U. & PISMEN, L. M. 2012 The relation of steady evaporating drops fed by an influx and freely evaporating drops. *J. Engng Maths* **73** (1), 17–30.

TREFETHEN, L. N. 2000 *Spectral Methods in MATLAB*. SIAM.

TSOUMPAS, Y., DEHAECK, S., REDNIKOV, A. & COLINET, P. 2015 Effect of Marangoni flows on the shape of thin sessile droplets evaporating into air. *Langmuir* **31** (49), 13334–13340.

VELLINGIRI, R., SAVVA, N. & KALLIADASIS, S. 2011 Droplet spreading on chemically heterogeneous substrates. *Phys. Rev.* E **84** (3), 036305.

VOINOV, O. V. 1976 Hydrodynamics of wetting. *Fluid Dyn.* **11** (5), 714–721.

WAYNER, P. C., KAO, Y. K. & LACROIX, L. V. 1976 The interline heat-transfer coefficient of an evaporating wetting film. *Intl J. Heat Mass Transfer* **19** (5), 487–492.

WU, Q. & WONG, H. 2004 A slope-dependent disjoining pressure for non-zero contact angles. *J. Fluid Mech.* **506**, 157–185.

XU, F. & JENSEN, O. E. 2016 Drop spreading with random viscosity. *Proc. R. Soc. Lond.* A **472** (2194), 20160270.

YI, T. & WONG, H. 2007 Theory of slope-dependent disjoining pressure with application to Lennard–Jones liquid films. *J. Colloid Interface Sci.* **313** (2), 579–591.

ZHENG, L., WANG, Y.-X., PLAWSKY, J. L. & WAYNER, P. C. 2002 Effect of curvature, contact angle, and interfacial subcooling on contact line spreading in a microdrop in dropwise condensation. *Langmuir* **18** (13), 5170–5177.